Spring 2018

Design for optical metamaterial design for optical metamaterial absorber

Huixu Deng

Department: Mechanical and Aerospace Engineering

DESIGN FOR OPTICAL METAMATERIAL ABSORBER

by

HUIXU DENG

A DISSERTATION

Presented to the Faculty of the Graduate School of the

MISSOURI UNIVERSITY OF SCIENCE AND TECHNOLOGY

In Partial Fulfillment of the Requirements for the Degree

DOCTOR OF PHILOSOPHY

in

MECHANICAL ENGINEERING

2018

Approved

Xiaodong Yang, Advisor
Jie Gao
Heng Pan
Edward C. Kinzel
Alexey Yamilov

PUBLICATION DISSERTATION OPTION

This dissertation consists of the following four articles that have been published or submitted for publication as follows:

Pages 9-19 have been accepted for publication in Journal of Optics.

Pages 20-38 have been accepted for publication in Optics Letters.

Pages 39-54 have been accepted for publication in Optics Express.

Pages 55-69 are intended for submission to Optics Express.

ABSTRACT

Optical metamaterial (MM) absorbers in the visible or near-infrared range have been widely investigated in these years since they are crucial in many promising applications, such as solar energy harvesting systems, thermo-photovoltaic energy conversion devices, thermal imaging and emissivity control. This dissertation aims to design and investigate various optical metamaterial absorbers based on different mechanisms and theories, such as cavity resonance, impedance match, equivalent circuit model and waveguide stop light mode. First, via utilizing the cavity resonance, a tunable narrowband MM absorber/emitter for thermophotovoltaic (TPV) is designed and analyzed based on gold nanowire cavities to improve the overall efficiency of TPV systems. Second, a broadband absorber made of ultrathin silica-chromium-silica film working in visible and near-infrared (NIR) range is proposed and demonstrated using impedance transformation method. To further broaden the absorption range and enhance the absorption performance, another broadband absorber covering the visible and near-infrared (NIR) is proposed firstly utilizing the combination of the multilayer impedance match in the short wavelength range and the double resonances in the long wavelength range. Finally, an ultra-broadband multilayer waveguide absorber is designed and studied via the stop light trapped at different waveguide width. The stop light mode is analyzed based on the waveguide mode theory considering the guided forward mode and backward mode at the same waveguide width position.

ACKNOWLEDGMENTS

First and foremost, I would like to express my sincere gratitude to my advisor, Dr. Xiaodong Yang, and my co-advisor, Dr. Jie Gao, for their encouragement, insightful guidance, and support during my Ph.D. study at Missouri University of Science and Technology. Their diligence and rigorous altitude to research and work will have a significant influence on my life. It has been a privilege and a great honor to have worked with them.

I would also like to extend my appreciation to all my dissertation committee members, Dr. Heng Pan, Dr. Edward C. Kinzel and Dr. Alexey Yamilov. Without their guidance and valuable comments, it would have been impossible for me to complete my dissertation.

This dissertation was supported by the Nanoscale Optics Laboratory and the Nanophotonics Laboratory at Missouri S&T, which are gratefully acknowledged.

I would like to express my deep thanks to my lab-mates and friends, Dr. Lei Sun, Dr. Yingran He and Mr. Wei Wang for their support during my study in Rolla.

Last but not the least, I wish to extend my special and sincere thanks to my parents, Mr. Shuhong Deng and Ms. Zhenyun Bao and all my family members for their love and unwavering support.

TABLE OF CONTENTS

LIST OF ILLUSTRATIONS

SECTION Page

PAPER IV

SECTION

1. INTRODUCTION

1.1. BACKGROUND

The term "metamaterial" (MM) is used by Walser in 2001 for the first time [1]. Wasler defined "metamaterial" as "macroscopic composites having a man-made, three-dimensional, periodic cellular architecture designed to produce an optimized combination, not available in nature, of two or more responses to a specific excitation". More sophisticated definition is given by Defense Advanced Research Projects Agency, USA, as "Metamaterials are a new class of ordered composites that exhibit exceptional properties not readily observed in nature" [2]. The prefix "meta" comes from Greek, meaning "after or beyond". Therefore, MMs can possess novel properties which cannot be easily attainable from natural materials. Recently, people like to use a simpler definition; MMs are artificial media structured on a size scale smaller than the wavelength of external stimuli [3, 4].

In MMs, a large branch of MM has garnered interest due to its applications in various fields from microwave (GHz) to optical (IR & visible). Initial interests in electromagnetic wave absorbers were largely in the microwave range, improving radar performance and providing concealment against others' radar systems in military [5]. Two well-known scientists who developed EM absorbers were W. W. Salisbury and J. Jaumann [6, 7]. Salisbury created the Salisbury screen which is a basic example of the resonant absorber. The absorber designed by Jaumann can conceptually be considered an extension of the Salisbury screen, acting as a resonant absorber over multiple wavelengths and achieving a broadband response [8-10].

The operating frequency range determines the applications of the MM absorber (as shown in Figure 1.1) including: radar system, stealth aircraft in gigahertz (GHz); biomedical imaging [11], environmental monitoring of earth [12], remote sensing of explosives [13], and spectroscopic characterization [14, 15] in terahertz (THz); thermal emitters, solar-energy harvesting (photovoltaics), and wireless communication in infrared (IR) & visible.

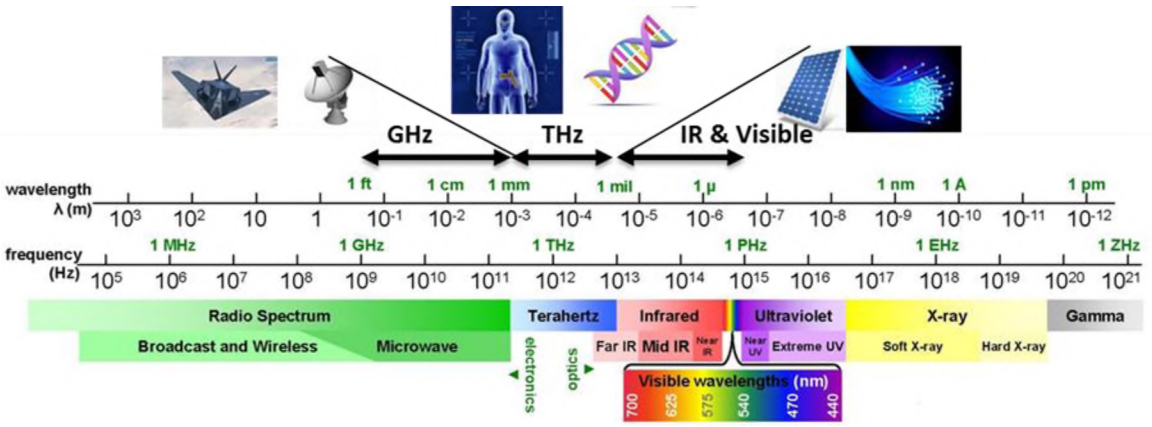

Figure 1.1. The electromagnetic spectrum with applications located in GHz, THz and IR & visible ranges. Copyright (2006) Southwestern Universities Research Association.

1.1.1 MM Absorber Operating in Different Frequency Ranges. In the infrared, optical and ultraviolet spectral range, the photon is the principal particle and fundamental concept that governs interactions between materials and EM waves, whereas at gigahertz frequencies major electron oscillations in the material are best amenable to describe material-EM wave interactions. Thus, the operating frequency range not only determines the applications of the MM absorber, but also its design principles and fabrication requirements as well, since the working frequency decides the size scale of the absorber structures and under different scale, material properties and fabrication techniques are dramatically different.

1.1.2 GHz Range – The First MM Perfect Absorber. GHz MM absorbers were initially used in radar system and much easier to be fabricated compared with the other MM absorbers since GHz is typically larger than 1mm. As the first of the MM perfect absorber, Landy et al. [16] theoretically and experimentally reported it in the GHz range, which was composed of conducting electric resonators on both front and rear sides of a dielectric substrate (as shown in Figure 1.2(a)). As shown in Figure 1.2(b), the obtained absorption has a peak with amplitude of 96% at 11.48 GHz and 88% at 11.5 GHz. Their results theoretically demonstrated that the origins of the absorption mechanism could be investigated for two reasons; the Ohmic surface loss and the dielectric loss outside the conductor. The latter loss occurs in between two MM elements where the electric field is large. Their structure turns out to be typical by fabricating two metallic layers: the first patterned metallic layer is for the minimized reflectance of EM wave by impedance

matching with the incident medium, and the role of second metallic layer is for blocking the transmission, usually made of continuous metallic layer.

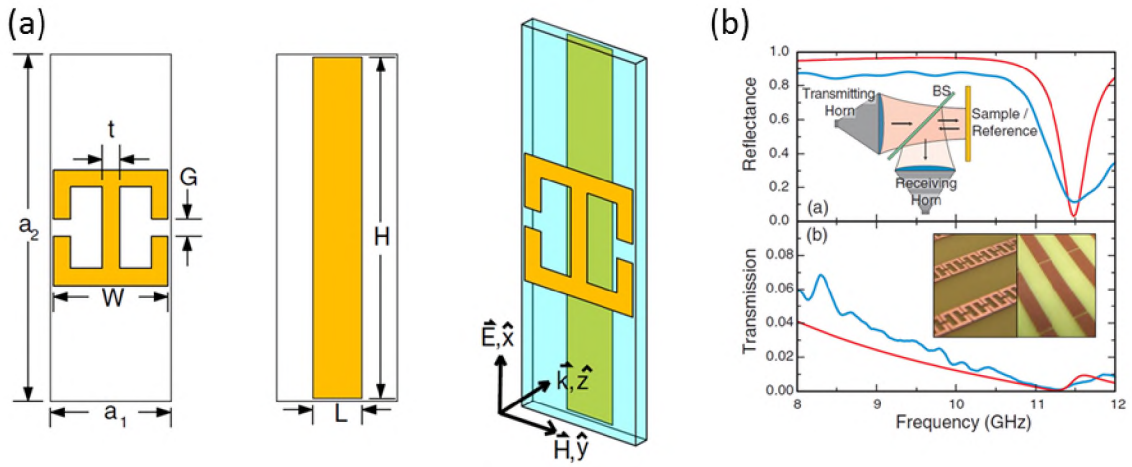

Figure 1.2. The first GHz absorber. (a) Schematic illustration of the first GHz absorber. (b) Simulated (red lines) and measured (blue lines) transmission and reflection [16].

1.1.3 THz Range – Subwavelength Frequency Selective Surface (FSS). THz electromagnetic (EM) waves, with a frequency ranging from 0.1 THz up to 10 THz, share common properties with GHz EM waves. Like micro- and millimeter waves, THz radiation can penetrate through a wide variety of non-conducting materials such as fabric, paper, plastic and wood. THz radiation is also non-ionizing and can be absorbed by molecules such as water and DNA. Additionally, since biological molecules exhibit a number of intermolecular and intramolecular modes with resonance frequencies in the THz regime, THz waves are expected to be able to interact with and reveal them with a certain degree of specificity [17]. These characteristics of THz waves make them suitable for a growing number of potential applications in biomedical imaging, environmental monitoring of earth, remote sensing of explosives, and semiconductor spectroscopic characterization.

As shown in Figures 1.3(a, b), similar to GHz MM absorber, THz MM absorber basically consists of a three layer system that includes a subwavelength frequency selective surface (FSS) layer, a dielectric spacer followed by a metallic back layer. The FSS is inspired by an electric-LC (ELC) resonator [18] which was capable of creating a

medium with a desired electric permittivity, followed by a metallic rod that was also used as the metallic back plane. FSS structures can be designed based on an electric dipole or multipole creation on the metallic rings, rods and crosses or even by groove-like void patterns in metal [19, 20], or a combination of these [21] (as shown Figure 1.3(c)) to get multi-band or broadband absorption.

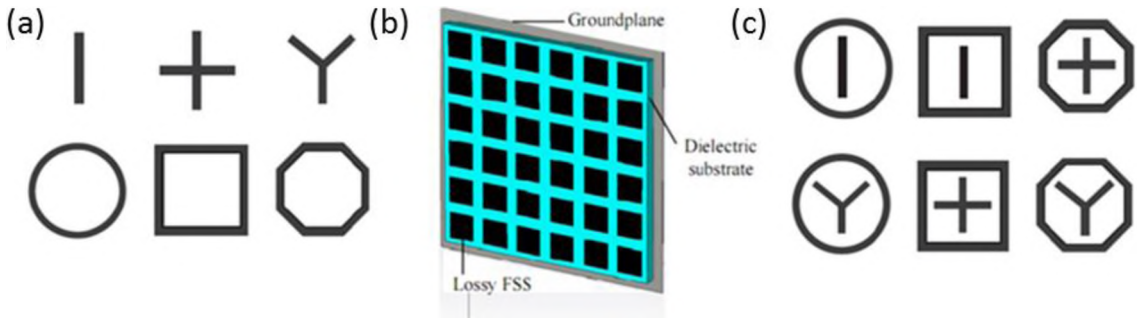

Figure 1.3. Schematic illustration of multipole and void FSS. Dark and green colors represent metal and dielectric, respectively: a) rod, ring, cross and Y shape FSS; b) FSS composed of void in a metal; and c) combination of different types of FSS [18].

The fundamental objective of design is to essentially realize a THz metamaterial antireflection coating device which is impedance matched with air and without any transmission through engineering proper FSS and dielectric spacer [22, 23]. Besides FSS, many papers have also proposed different ideas about the physical mechanism underlying the MM THz absorbers based on anti-parallel currents [24], out of phase currents [25] inside the absorber or according to the standing waves resonances inside the spacer [26], as well as destructive interference between the reflected waves of the FSS and the metallic back layer [27].

Soon after the first demonstration of THz absorber, different structures have been fabricated to enhance the functionality of the device, including achieving polarization independence [28, 29], dual band [28, 30], triple band [29, 31], multi band [26, 32], and broadband perfect absorbers [33-37]. Tunability of the absorption frequency via different methods has also been investigated [38-43].

1.1.4 IR & Visible Range – Selective Solar Absorption. Applications utilizing solar energy are being actively developed due to increasing demand for environmentally friendly and sustainable energy solutions. The sun is a source of tremendous energy

spanning from ultraviolet to infrared wavelengths, with the maximum energy in the visible range, corresponding to a blackbody temperature of 5780 K [44]. One of the better-known means of harnessing solar energy is photovoltaics (Figure 1.4(a)), where solar radiation is converted into electricity with the help of various semiconducting materials, exhibiting the photovoltaic effect and referred to as solar or photovoltaic cells [45, 46]. Exposure of the solar cell to light triggers the generation of electron–hole pairs, carrying an electric current, thus the system is dependent on the band structure of the corresponding material. The light incident on a photovoltaic cell, however, is not required to originate from the sun. In the field of thermophotovoltaics (TPV) (Figure 1.4(b)), a thermal emitter heated to a high temperature serves as a source of radiation [47, 48]. Solar TPVs (Figure 1.4(c)) use solar energy to heat the emitter and take advantage of concentrators that focus the radiation collected over a larger area onto a much smaller photovoltaic system, thus reducing the material costs. Solar thermal systems (Figure 1.4(d)) use solar radiation to create heat, which can be used directly for applications including industrial processes or absorption cooling [49]. Since low IR emittance becomes especially important for higher temperature applications due to the T4 dependence of radiative losses. Thus, there has been a recent push to develop engineered structures and materials with spectral selectivity in their absorption and emission profiles that withstand high temperatures.

In addition, the broadband response design is mainly focused on. One of the approaches to achieve a broadband response is to combine a number of resonators of various sizes in a multi-unit of resonators. Examples of this approach can be found in the structures shown in Figures 1.4(e, f). A sublattice of 16 individual metamaterial cross elements based on a Au/Al2O3/Au stack was designed to operate in the range of 0.5–1.8 μm in order to match the bandgap of a gallium antimonide solar cell (Figure 1.4(e)) [50]. The total size of the combined lattice was 1080 nm with individual crosses of linewidth 20 nm. A very accurate match of not only the wavelength range, but also the magnitudes corresponding to various wavelengths has been achieved due to the capabilities of this method. In addition, a combination of tungsten patches of various sizes has been used to predict close to 100% absorption throughout the solar operation range (Figure 1.4(f))

[51]. Starting with the simpler structure of just two different slab sizes, the effects of all geometrical parameters on the performance of the of the absorber were investigated.

Experimental demonstrations of similar dual-size slab Au/ZnS/Au structures can be found in Ref. 52, showing a broadband response over the 7.58–9.47 μm range. The limitations of this approach are the limited number of resonator sizes that can be utilized within one period of the structure, as well as the larger size of the combined unit cell relative to the wavelength of incident radiation. The fraction of surface area occupied by each resonator of a particular size within a given unit cell is reduced as the number of resonator sizes per unit cell is increased. This leads to a trade-off between bandwidth and absolute absorption efficiency.

1.1.5 Applications of MM Absorber. The flexibility of MM absorbers in GHz, by employing ink-jet printing, has been pursued recently. On the other hand, inks of more kinds of electrical conductivity should be prepared to realize high-performance flexible MM absorbers, and the reproducibility of the process also matters. The flexibility continues to be the issue for other frequency ranges, such as THz and IR & visible, and furthermore, the flexible MM absorbers made by simpler fabrication processes come to be achieved.

The optimized MM absorbers in the THz region could work as improved detectors for imaging and detecting the harmful elements to human, and for detecting heat in enhanced and spectrally selective way. The match of MM absorbers in the THz region makes the relevant important applications of special interest worldwide, which comprises non-destructive quality and process control and environmental monitoring implementations [53]. On some of these devices, more sophisticated characteristics such as tunability, multi-band or broadband spectral response, and incident-angle- and/or polarization-independent responses should be demonstrated in the future.

MM absorbers in IR & visible frequency range keeps being studied [54]. The absorption mechanism is being further elucidated. Not only the interference theory can explain the broadband perfect absorption, and in parallel, plasmonic coupling and multi-excitation of plasmon resonance due to the reflective nature of copper base film, also contribute to the high absorption of the structure. Owing to the simple fabrication technique, the production cost is very low compared with the competitive methods such

as e-beam lithography. In addition, the higher fabrication tolerance makes it an outstanding candidate for future application in photovoltaic and sensors.

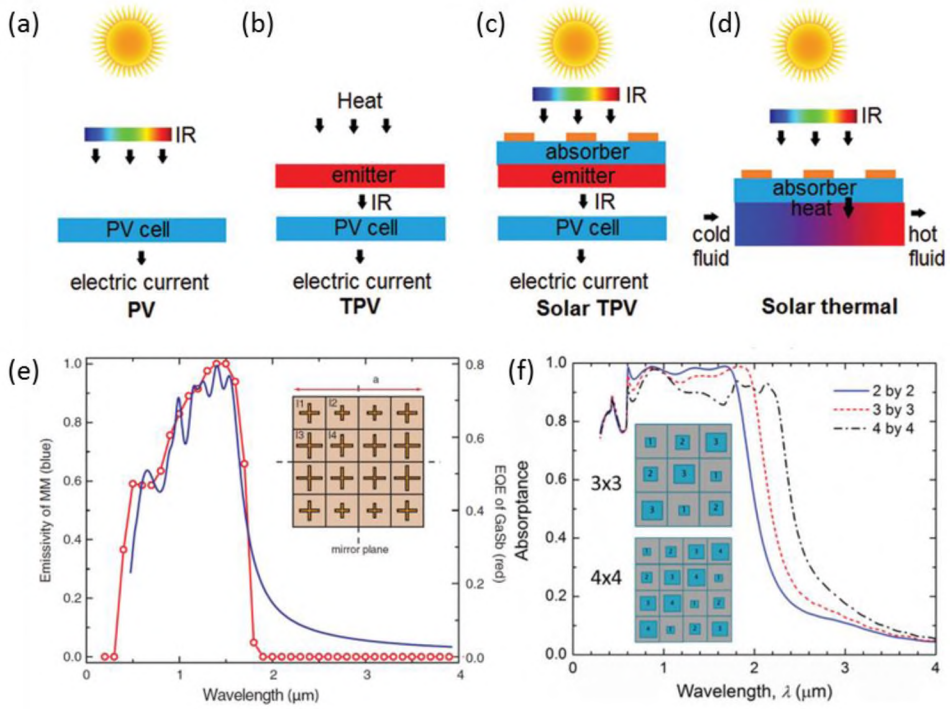

Figure 1.4. Solar energy conversion systems schematics: (a) photovoltaic system, (b) thermophotovoltaic system, (c) solar thermophotovoltaic system, (d) solar thermal system [45-49]. Broadband multi-unit MM absorbers: (e) unit cell with multisized crosses, (f) unit cell with multisized squares [50-52].

MM absorbers operating in GHz, THz and IR & visible ranges need simpler design, easier fabrication, lower production cost, and higher fabrication tolerance. As we move upward in the design stack to more complex components and devices, new emergent phenomena and more complex functionalities might be synthesized at each level, paving the way to a new era for MM absorbers [55].

1.2. RESEARCH OBJECTIVES

This research aims at the creation of new knowledge in the understanding of optical metamaterial absorbers based on different mechanisms. Each design mechanism makes the absorber tunable and controllable due to the accurate prediction in theory and simulation. The developed models and equations can guide the designing procedure and

provide a new way to further enhance the absorber performance. For the narrowband nanowire cavity absorber for TPV, effective media theory is used and the absorption peak can be tuned according to the finite element simulation results. For the broadband SiO2-Cr-SiO2 multilayer absorber, the impedance transformation matrix is utilized to determine the thickness of each layer thickness and maximize the absorption range. It can also guide the design in the same way to further broaden the absorption range and give out the limits of this sort of absorber. To achieve ultrabroadband absorption covering the visible and NIR range, the double ring absorber is designed based on the equivalent circuit model. It is the first time to combine the impedance match condition in short wavelength and coupled resonance in long wavelength to broaden the absorption range. Finally, the waveguide absorber consisting of 13-pair of Au and SiO2 is also demonstrated to be ultrabroadband due to the waveguide stop-light mode obtained at different waveguide positions.

PAPER

I. IMETAMATERIAL THERMAL EMITTERS BASED ON NANOWIRE CAVITIES FOR HIGH-EFFICIENCY THERMOPHOTOVOLTAICS

Huixu Deng, Tianchen Wang, and Xiaodong Yang

Department of Mechanical and Aerospace Engineering,

Missouri University of Science and Technology, Rolla, Missouri 65409

ABSTRACT

Metamaterial thermal emitters based on gold nanowire cavities on a gold substrate are designed to achieve narrowband emission spectrum with the emission peak located slightly above the bandgap of photovoltaic (PV) cells, in order to improve the overall efficiency of thermophotovoltaic (TPV) systems. The metamaterial emitter made of gold nanowires embedded in alumina host exhibits an effective permittivity with extreme anisotropy, which supports cavity resonant modes of both electric dipole and magnetic dipole. The impedance match between the cavity modes and free space leads to strong thermal emission with the desired frequency range slightly above the bandgap of PV cells. Simulation results show that the designed metamaterial emitters are polarization-insensitive and have nearly omnidirectional emission angles. Moreover, theoretical analysis predicts that the overall efficiency of the TPV system can reach Shockley-Queisser limit at a low emitter temperature of T_e = 940 K.

Keywords: Energy transfer, Metamaterials, Subwavelength structures

1. INTRODUCTION

Metamaterials with artificial structured composites can exhibit intriguing electromagnetic phenomena, such as negative refraction [1], invisible cloaking [2], near-zero permittivity [3], and indefinite cavities [4, 5]. The macroscopic properties of metamaterials can be tailored flexibly by designing the artificial meta-atoms. Metamaterial absorbers and emitters working at THz and infrared frequency range have

been designed and demonstrated recently [6-12], which hold great promise in light harvesting, thermal detection and electromagnetic energy conversion. In the application of thermal energy harvesting using photovoltaic (PV) cells, the main challenge is to improve the efficiency of thermophotovoltaic (TPV) systems in which the energy conversion process is from heat to electricity via photons. The maximum efficiency is defined by Shockley-Queisser (SQ) limit, which arises mainly from two loss mechanisms: on one hand, photons incident on the PV cells with energy lower than the PV cell bandgap energy will not be absorbed by the PV cell and lost in free space; on the other hand, photons with energy above the bandgap energy can be absorbed, but the excess energy will be lost in generating undesirable heat. An effective way to avoid these two kinds of loss is to design a thermal emitter with resonance frequency located slightly above the PV cell bandgap energy and narrow emission spectrum bandwidth.

In this paper, a thermal emitter based on metamaterial nanowire cavities is investigated in order to improve the overall efficiency of TPV systems. The unit cell of this thermal emitter with a period of P=600 nm is shown in Figure 1(b), and consists of two elements: the nanowire cavities array and the 140 nm thick gold substrate as a metallic mirror. The cavity is made of 6 by 6 gold nanowires with radius r0 and center-to-center distance D=60 nm embedded in alumina host which forms a cube with L=360 nm and h=140 nm. To model the thermal emitter in Finite-Element Method simulation, the permittivity of gold is described by Drude model: $\varepsilon_m(\omega)=1-\omega_p^2/\omega(\omega+i\gamma_0)$, where ω is the frequency, $\omega_p=1.37\times10^{16}$ rad/s is the plasma frequency and $\gamma_0=4.08\times10^{13}$ rad/s is the bulk collision frequency, while the permittivity of alumina is $\varepsilon_d=3.0625$. From the simulation results, the absorption spectrum α can be obtained by $\alpha=1-R$ since only the reflection spectrum R can be calculated in simulation and the transmission is zero due to the thick gold substrate. In addition, according to Kirchhoff's law of thermal radiation, at thermal equilibrium, the absorption is equal to the emission, $\xi=\alpha$, for every frequency, direction and polarization. Thus, the emission behaviors of the thermal emitter can be unveiled based on the absorption spectrum.

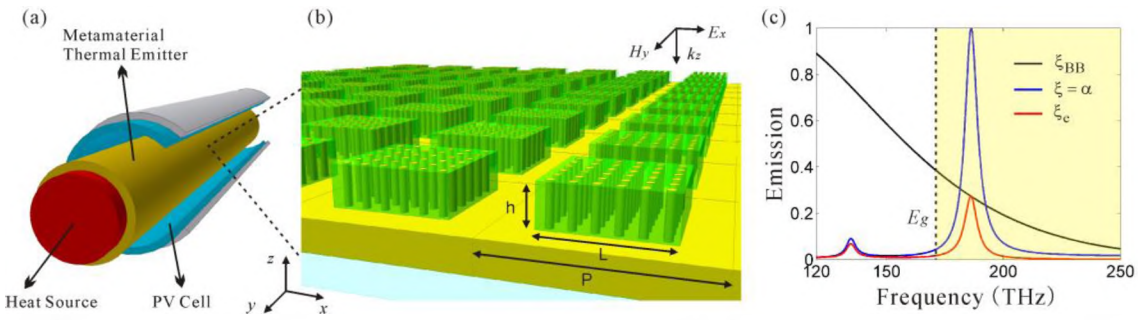

Figure 1. Schematic of the TPV system and the emission spectra of the metamaterial emitter. (a) The TPV system mainly includes three components: the heat source to provide thermal energy, the thermal emitter to emit photons at specific frequency and the PV cell to collect photons and generate electricity. (b) The structure of the metamaterial thermal emitter made of gold nanowires embedded in alumina host. (c) The simulated emission spectra where the yellow area is above the bandgap and represents the photons that can be absorbed by the PV cell.

The emission spectrum of the thermal emitter is shown as the blue curve in Figure 1(c), where the radius of the nanowire is r0=12.5 nm and normal incidence is applied. It can be seen that the main emission peak of almost 100% is achieved at the frequency of 187 THz. The normalized emission spectrum of ideal blackbody ξ_{BB} is also presented as the black curve in Figure 1(c) at the temperature of T=940 K. And the thermal emissivity of the emitter Ee at T=940 K can be obtained by $E_e = \xi_{BB} \times \xi$ as the red curve in Figure 1(c). Actually, the emission spectrum can be also calculated using the effective medium theory (EMT) by regarding the nanowire cavity as an anisotropic medium with the following permittivity components [13],

$$\varepsilon_x = \varepsilon_y = \varepsilon_d \frac{(1+f_m)\varepsilon_m + (1-f_m)\varepsilon_d}{(1-f_m)\varepsilon_m + (1+f_m)\varepsilon_d}, \quad \varepsilon_z = f_m \varepsilon_m + (1-f_m)\varepsilon_d, \tag{1}$$

where $f_m = \pi r_0^2 / D^2$ is the volume filling ratio of gold nanowires.

2. ANALYSIS OF THE THERMAL EMITTER

In order to gain further insight into how the nanowire cavity enhances the thermal emission, the electric and magnetic fields are simulated in the structure which is excited by a normally incident plane wave at the resonant frequency. Figures 2(a) and 2(b) show

the magnetic field profile H_y and the electric filed profile E_x in the x-z plane, respectively. The mechanism of high emission for the thermal emitter on resonance can be understood as the cavity supports electric dipole resonance and magnetic dipole resonance simultaneously. The electric dipole resonance can be observed from the accumulation of polarized positive charges and negative charges at the top left and top right corners of the cavity [Figure 2(c)] by calculating the divergence of the electric field ($\nabla \cdot \boldsymbol{E} = \rho / \varepsilon_0$, where ρ is the polarized charge density). Additionally, the magnetic dipole resonance can be seen from the anti-parallel displacement current [$\partial D / \partial t = -i\omega D = -i\omega\varepsilon E$, Figure 2(d)] formed between the nanowire cavity and the gold substrate due to the large negative permittivity of metal.

To analyze the high emission on resonance quantitatively, effective permittivity and permeability of the structure are retrieved to obtain the impedance, by using the method described by Ref. [14]. from which the condition of impedance match to the free space can be achieved. With the calculated reflection (S11) and transmission (S21), the impedance z can be written as:

$$z = \sqrt{\frac{\mu_{eff}}{\varepsilon_{eff}}} = \pm\sqrt{\frac{\left(1+S_{11}\right)^2 - S_{21}^2}{\left(1-S_{11}\right)^2 - S_{21}^2}} \tag{2}$$

At the resonance of cavity mode, $z = 0.976 + 0.017i$, which perfectly match the free space impedance z0. The corresponding effective permittivity and permeability are ε_{eff}=0.638+2.850i and $\mu_{eff} = 0.513 + 2.735i$, respectively, for the cavity mode shown in Figure 2.

To ensure the emission resonant frequency is slightly above the bandgap energy for different PV cells, the geometries of the thermal emitter can be tuned accordingly. In the current design, the cavity height h and the filling ratio f_m are tuned to adjust both the resonant frequency position and the impedance match condition, in order to achieve high-efficiency TPV system. Figures 3(a) and 3(b) show the dependence of emission spectra on the cavity height h and the filling ratio f_m at normal incidence, respectively. To optimize the TPV system efficiency, the cavity height h=140 nm and the filling ratio

f_m=14% are used for the PV cell of GaSb (with the bandgap energy of E_g=0.71eV). Note that the nanowire cavity can be designed for different PV cells with certain bandgap energy by simply tuning the cavity geometry.

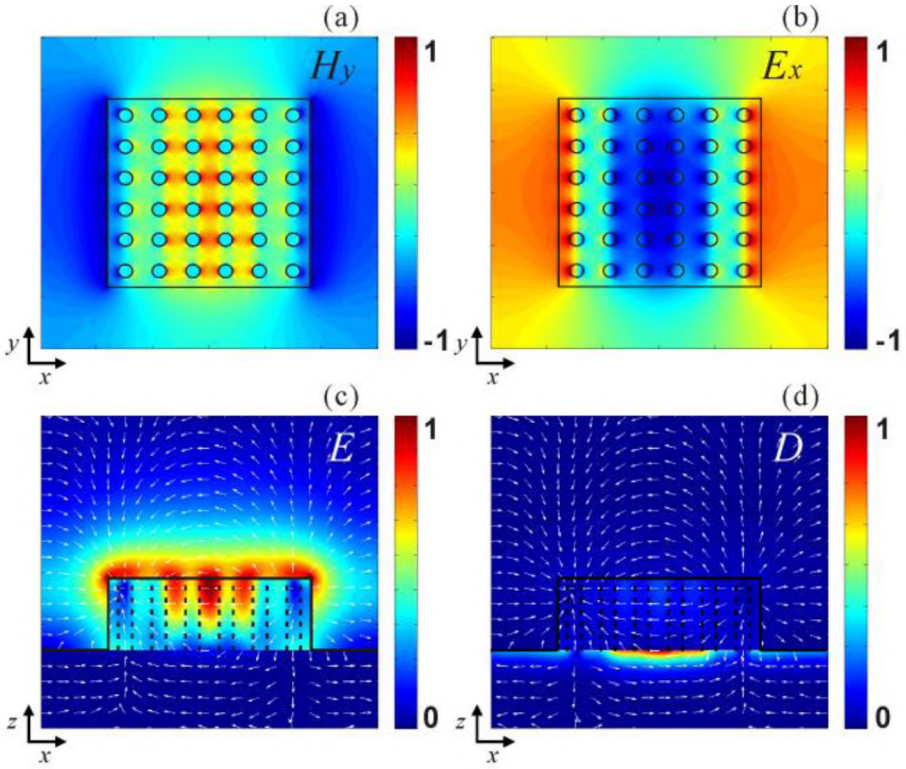

Figure 2. Resonant field profiles. (a) and (b) are the magnetic field profile and the electric field profile of the nanowire cavity in the x-y plane, respectively. (c) The intensity and direction of the electric field distribution and (d) the displacement current distribution in the x-z plane.

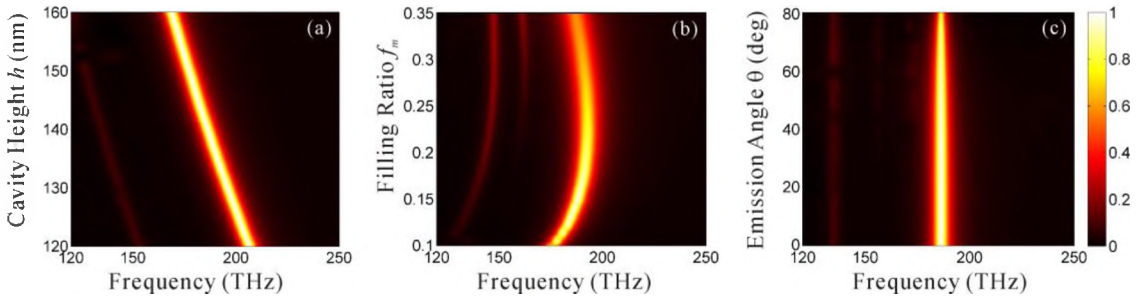

Figure 3. Emission spectra of the nanowire cavity.(a) and (b) show the dependence of emission spectra on the cavity height h and the metal filling ratio f_m at normal emission angle, respectively. (c) The average of both the TE and TM emission spectra, $\xi = \left(\xi_{\mathrm{TE}} + \xi_{\mathrm{TM}}\right)/2$, which is taken as the actual emission of the thermal emitter.

Furthermore, the designed thermal emitter is polarization-insensitive and nearly omnidirectional for all the emission angles. It is polarization-independent since the nanowire cavity possesses 4-fold rotation symmetry in the x-y plane. For oblique incidence, the emission spectra of both polarizations [transverse electric (TE) polarization and transverse magnetic (TM) polarization] are almost the same so that the average of both the TE and TM emission spectra, $\xi = (\xi_{\mathrm{TE}} + \xi_{\mathrm{TM}})/2$, is taken as the actual emission of the thermal emitter as shown in Figure 3(c). As the emission angle increases up to 80° for both TE and TM, the frequency of emission peak remains the same and the emission strength always keeps at a high level.

3. EFFICIENCY OF THE TPV SYSTEM

To evaluate the performance of the metamaterial thermal emitter made of nanowire cavities for TPV systems, the overall system efficiency is theoretically calculated. In general, the maximum efficiency of a system is limited by the Carnot efficiency (all heat energy is converted to electrical energy without loss) which can be given by $\eta_{car} = 1 - T_c / T_e$. When the temperature of the PV cell collector Tc is 300 K and the temperature of the emitter T_e is maintained at 1000 K, a maximum efficiency of 70% can be obtained. However, for TPV systems, efficiencies are limited by other factors in the energy conversion process from heat to electricity via photons. Following the analysis by Shockley and Queisser [15], the overall energy conversion efficiency of TPVs is:

$$\eta = U(T, E_g) \times \nu(T, E_g) \times m(V_{op}) \tag{3}$$

where U is the "ultimate efficiency", which is proportional to the energy contained in photon-excited electron-hole pairs divided by the incident radiation energy, v is an efficiency due to recombination process which means charge carries may be removed from the PV cell in additional ways, and finally m is called "impedance mismatch" efficiency caused by the difference between the open circuit voltage V_{op} and the optimal operating voltage.

According to the assumption that one photon with energy larger than the PV cell bandgap energy E_g will excite one electron-hole pair resulting in the contribution of E_g electricity energy to the TPV system, the ultimate efficiency can be achieved by calculating the energy carried by excited electron-hole pairs with respect to the incident radiation energy [15, 16]:

$$U = \frac{\int_0^{\pi/2} d\theta \sin(2\theta) \int_{E_g}^{\infty} dE \xi(E,\theta) I_{BB}(E,T_e) \frac{E_g}{E}}{\int_0^{\pi/2} d\theta \sin(2\theta) \int_0^{\infty} dE \xi(E,\theta) I_{BB}(E,T_e)} \tag{4}$$

In this equation, the denominator is the incident radiation energy onto the PV cell, which is equal to the thermal emission energy from the emitter calculated by the integral of blackbody radiation IBB (when the emitter temperature is T_e) multiplying the emission of the emitter at all emission angles θ (assuming the emitter to be planar with no azimuthal angular dependence). The numerator is the energy contained in excited electron-hole pairs by cutting off the photon energy below E_g and reducing the higher photon energy into E_g . In order to average the emission in both TE and TM polarizations, $\xi(E,\theta) = \xi_{\mathrm{TE}}(E,\theta)/2 + \xi_{\mathrm{TM}}(E,\theta)/2$ is considered.

Besides the efficiency of creating excited electron-hole pairs, the recombination efficiency v is utilized to measure the percent of charge carriers becoming the desired external current. And it can be expressed as the ratio between the open circuit voltage V_{op} and the initial material bandgap voltage $V_g = E_g / q$, in which q is the charge of one electron [16, 17]:

$$\nu = \frac{V_{op}}{V_g} = \frac{V_c}{V_g} \ln\left(f \frac{Q_e(T,E_g)}{Q_c(T_c,E_g)} \right) \tag{5}$$

where $V_c = k_B T_c / q$ is the voltage of the PV cell related to the cell temperature T_c. Q_e and Q_c are photon number flux incident on the PV cell from the emitter, and from an ideal blackbody surrounding the cell at the same temperature of the PV cell T_c, respectively [16]. Here, f is chosen as 0.5 for an ideal case when both the emitter and the cell have planar geometries.

The third factor in Eq. (3), m(V_{op}), is evaluated when the operating voltage Vmax is chosen to maximize the electrical power for the PV cell [16],

$$m\left(V_{op}\right) = \frac{z_m^2}{\left(1 + z_m - e^{-z_m}\right)\left(z_m + \ln\left(1 + z_m\right)\right)} \tag{6}$$

with z_m determined by the ratio between V_{max} and V_c and related to $V_{op} / V_c = z_m + \ln\left(1 + z_m\right)$.

When the filling ratio of nanowire is $f_m = 0.14$, each efficiency factor in Eq. (3), U, v and m, is calculated as functions of the PV cell's bandgap energy E_g and the temperature of the emitter T_e. v and m are both determined by the properties of PV cell. U and η are enhanced by the designed thermal emitter as shown in Figure 4. The resonant frequency of the emitter is tuned to 187 THz and the emitter temperature is set at about $T_e = 940$ K to reach the SQ limit of $\eta_{SQ} = 0.31$. The emitter temperature required to reach the SQ limit is much lower than the temperature of 2500 K in current existing solar TPV systems. If the temperature is too low, the efficiency will be reduced due to the decrease of v and m. When the temperature increases, the efficiency can even get higher and exceed the SQ limit, but it is limited by the melting point of the emitter materials [18]. The melting temperature of gold is around 1337 K, which is much higher than the current operation emitter temperature of 940 K. In the future, new design of emitters with high melting point materials can improve the overall efficiency furthermore.

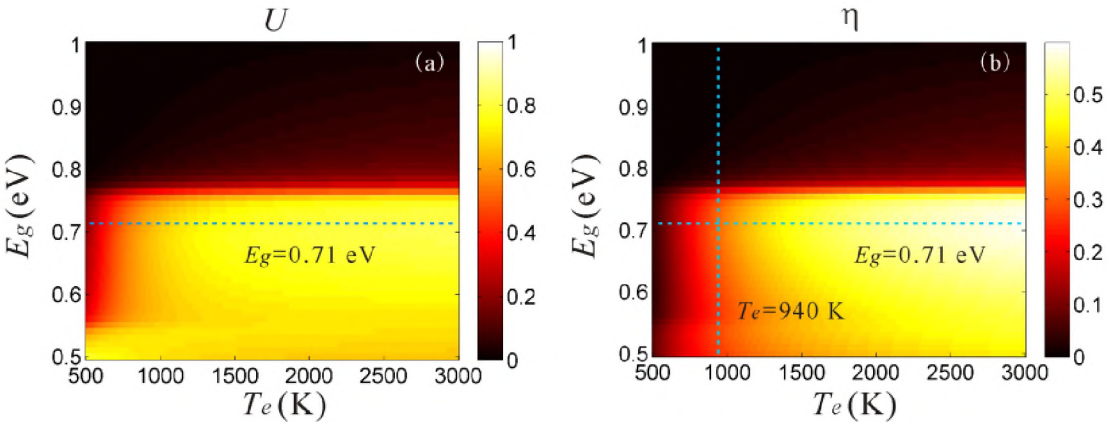

Figure 4. Theoretical calculation of the TPV system efficiency as a function of the PV cell bandgap energy E_g and the emitter temperature T_e. (a) The ultimate efficiency U, where the dashed line represents the bandgap energy of GaSb with $E_g = 0.71$ eV. (b) The overall conversion efficiency, $\eta = U \times \nu \times m$, which can reach the SQ limit of 0.31 when the PV cell is GaSb and the emitter temperature is relatively low at $T_e = 940$ K (represented by the vertical dashed line).

4. CONCLUSION

In conclusion, to improve the overall efficiency of TPV system, a metamaterial thermal emitter based on nanowire cavities is proposed and demonstrated. The cavity mode supports both the electric dipole resonance and the magnetic dipole resonance simultaneously. At the resonant frequency, the impedance of the metamaterial thermal emitter can match the impedance of the free space, resulting in high emissivity with narrow emission bandwidth. The resonant frequency can be tuned to match the bandgap energy of different PV cells by changing the cavity height as well as the filling ratio of gold nanowires. The emission as a function of different angles for both the TE and TM polarizations is also investigated for determining the efficiency of TPV systems. By tuning the emission frequency slightly above the bandgap energy of PV cell, the overall efficiency can reach SQ limit of $\eta_{SQ} = 0.31$ at a low emitter temperature of 940 K. When the emitter temperature is increased, the efficiency can exceed the SQ limit, but it is still limited by the melting point of the emitter materials.

ACKNOWLEDGMENT

This work was partially supported by the Intelligent Systems Center and the Energy Research and Development Center at Missouri S&T, the University of Missouri Interdisciplinary Intercampus Research Program, and the University of Missouri Research Board. The authors acknowledge Y. He and J. Gao for their helpful discussions about this work.

REFERENCES

[1] R. A. Shelby, D. R. Smith, and S. Schultz, "Experimental verification of a negative index of refraction," Science 292, 77-79 (2001).

[2] J. B. Pendry, D. Schurig, and D. R. Smith, "Controlling electromagnetic fields," Science 312, 1780-1782 (2006).

[3] A. Alù, M. G. Silveirinha, A. Salandrino, and N. Engheta, "Epsilon-near-zero metamaterials and electromagnetic sources: Tailoring the radiation phase pattern," Phys. Rev. B 75, 155410 (2007).

[4] X. Yang, J. Yao, J. Rho, X. Yin, and X. Zhang, "Experimental realization of three-dimensional indefinite cavities at the nanoscale with anomalous scaling laws," Nat. Photonics 6, 450-454 (2012).

[5] J. Yao, X. Yang, X. Yin, G. Bartal, and X. Zhang, "Three-dimensional nanometer-scale optical cavities of indefinite medium," Proc. Natl. Acad. Sci. U. S. A 108, 11327-11331 (2011).

[6] H. Tao, N. I. Landy, C. M. Bingham, X. Zhang, R. D. Averitt, and W. J. Padilla, "A metamaterial absorber for the terahertz regime: design, fabrication and characterization," Opt. Express 16, 7181-7188 (2008).

[7] N. Liu, M. Mesch, T. Weiss, M. Hentschel, and H. Giessen, "Infrared perfect absorber and its application as plasmonic sensor," Nano Lett. 10, 2342-2348 (2010).

[8] Y. Avitzour, Y. A. Urzhumov, and G. Shvets, "Wide-angle infrared absorber based on a negative-index plasmonic metamaterial," Phys. Rev. B 79, 045131 (2009).

[9] X. Liu, T. Tyler, T. Starr, A. F. Starr, N. M. Jokerst, and W. J. Padilla, "Taming the blackbody with infrared metamaterials as selective thermal emitters," Phys. Rev. Lett. 107, 045901 (2011).

[10] Y. Cui, K. H. Fung, J. Xu, H. Ma, Y. Jin, S. He, and N. X. Fang, "Ultrabroadband light absorption by a sawtooth anisotropic metamaterial slab," Nano Lett. 12, 1443-1447 (2012).

[11] I. Celanovic, D. Perreault, and J. Kassakian, "Resonant-cavity enhanced thermal emission," Phys. Rev. B 72, 075127 (2005).

[12] Y. He, H. Deng, X. Jiao, S. He, J. Gao, and X. Yang, "Infrared perfect absorber based on nanowire metamaterial cavities," Opt. lett. 38, 1179-1181 (2013).

[13] A. H. Sihvola, Electromagnetic Mixing Formulae and Applications (Iet, 1999).

[14] X. Chen, T. M. Grzegorczyk, B.-I. Wu, J. Pacheco, Jr., and J. A. Kong, "Robust method to retrieve the constitutive effective parameters of metamaterials," Phys. Rev. E 70, 016608 (2004).

[15] W. Shockley and H. J. Queisser, "Detailed balance limit of efficiency of p-n junction solar cells," J. Appl. Phys. 32, 510-519 (1961).

[16] E. Rephaeli and S. Fan, "Absorber and emitter for solar thermo-photovoltaic systems to achieve efficiency exceeding the Shockley-Queisser limit," Opt. Express 17, 15145-15159 (2009).

[17] W. Chihhui, N. Burton, III, J. Jeremy, M. Andrew, Z. Byron, S. Steve, and S. Gennady, "Metamaterial-based integrated plasmonic absorber/emitter for solar thermo-photovoltaic systems," J. Opt. 14, 024005 (2012).

[18] S. Molesky, C. J. Dewalt, and Z. Jacob, "High temperature epsilon-near-zero and epsilon-near-pole metamaterial emitters for thermophotovoltaics," Opt. Express 21, A96-A110 (2013).

II. BROADBAND PERFECT ABSORBER BASED ON ONE ULTRATHIN LAYER OF REFRACTORY METAL

Huixu Deng, Zhigang Li, Liliana Stan, Daniel Rosenmann, David Czaplewski, Jie Gao, and Xiaodong Yang

Department of Mechanical and Aerospace Engineering,

Missouri University of Science and Technology, Rolla, MO, 65401

ABSTRACT

An ultrathin 3-layer broadband absorber made of the refractory metal Cr without patterning is proposed. To guide the design, a theory based on the impedance transformation method is developed and a desired metal permittivity is derived to achieve the broadest and highest absorption simultaneously. Meanwhile, it is found that the permittivity of refractory metals, like Cr, is closest to the desired metal permittivity in the visible and near-infrared (NIR) range compared with noble metals or other metals. Thereupon, a 3-layer Cr-SiO_2 absorber sample is fabricated to demonstrate the broadband absorption in experiment. And its absorption can cover the range of $0.4-1.4\mu m$ with amplitude over 90%. It is also proved experimentally that the absorber is angle-insensitive, polarization-insensitive and omnidirectional. Furthermore, other than using refractory metals, the absorption can be even improved by adding more layers, reducing the metal layer thickness and filling the metal layer with other high loss materials. Due to the high melting point of refractory metals, the proposed broadband absorber can also act as emitter working at high temperature. A broadband perfect absorber based on one ultrathin layer of the refractory metal chromium without structure patterning is proposed and demonstrated. The ideal permittivity of the metal layer for achieving broadband perfect absorption is derived based on the impedance transformation method. Since the permittivity of the refractory metal chromium matches this ideal permittivity well in the visible and near-infrared range, a silica-chromium-silica three-layer absorber is fabricated to demonstrate the broadband perfect absorption. The experimental results under normal incidence show that the absorption is above 90% over the wavelength range of

$0.4-1.4\mu m$ and measurements under angled incidence within $400-800nm$ prove that the absorber is incident angle-insensitive and polarization-independent.

Keywords: Metamaterials; Absorption; Multilayer design; Thin films, optical properties.

1. INTRODUCTION

Broadband absorbers in the visible or near-infrared range have been widely investigated in these years [1, 2] since they are crucial in many promising applications, such as solar energy harvesting systems [3-5], thermo-photovoltaic energy conversion devices [6-12], thermal imaging [13-15] and emissivity control [16-18]. Recently, many efforts for designing broadband absorbers have been made based on different mechanisms. First of all, broadband absorption can be obtained by combining multiple resonances together which are located at distinct wavelengths. Typically, the excitation of multiple resonances can be achieved within metal-dielectric-metal (MIM) cavities by tuning the feature sizes of the localized resonators [16, 19-22]. Aydin et al. [21] demonstrated an ultrathin (260 nm) plasmonic super absorber consisting of a MIM stack with a nanostructured top silver film composed of crossed trapezoidal arrays. This sort of broadband absorber based on MIM stack is very thin with patterning on the top and usually operates in the visible range. Secondly, broadband absorbers can be also designed by exciting phase resonances based on the lattice scattering effect [23-25]. Wang et al. [23] proposed an efficient multiband absorber comprised of a truncated, one-dimensional periodic metal–dielectric photonic crystal and a reflective substrate. Thirdly, the impedance match mechanism can be utilized for designing broadband absorbers. Mattiucci et al. [26] proved an approach to tailor the absorbing characteristics based on the effective metamaterial properties of thin, periodic metal-dielectric multilayers. Its absorption is broad in the visible range and can be further expanded by adding more periodic layers. Finally, the excitation of slow light modes can be applied to broaden the absorption by employing the tapered multilayer waveguides [27-30]. Cui et al. [27] presented an ultrabroadband thin-film infrared absorber made of tapered anisotropic metamaterial waveguide which operates in the NIR range. For this type of broadband absorber, the tapered structure is necessary, and more layers can generally lead to broader

absorption since it can make the waveguide width cover wider range resulting in allowing more waveguide modes supported at different positions. In summary, broadband absorbers can be designed according to different mechanisms and those mechanisms can be generally realized experimentally by utilizing diverse metal-dielectric stacks with patterning. It is also found that noble metals are widely used in the absorbers since they are easy to be fabricated and with good optical properties in the visible and NIR range.

In this paper, an ultrathin 3-layer broadband absorber made of the refractory metal without patterning is proposed. Since the absorber only consists of three layers without patterning, it is very easy to fabricate. A theory based on the impedance transformation method is developed to analyze the absorber and a desired metal permittivity is derived to guide the design to obtain the broadest and highest absorption simultaneously. At the same time, it is found that the permittivity of refractory metals, like Cr, is closest to the desired metal permittivity in the visible and near-infrared (NIR) range compared with noble metals or other metals. So a 3-layer Cr-SiO_2 absorber sample is fabricated to demonstrate the broadband absorption in experiment. And its absorption can cover the range of $0.4-1.4\mu m$ with amplitude over 90%.

2. THEORIES AND METHODS

Figure 1(a) shows the schematic of the 3-layer absorber consisting of two dielectric layers (with permittivity of ε_d and thickness of d_d), one metal layer (with permittivity of ε_m and thickness of d_m) in the middle and a mirror substrate (with permittivity of ε_s and a large enough thickness to eliminate transmission, $T=0$) made of gold.

In order to investigate the absorption A of the whole structure which is only affected by the reflection R and equal to $A=1-R$ because of $T=0$, its wave impedance is calculated based on the impedance transformation method [31]:

$$Z(j)=Z_j\frac{Z(j+1)-iZ_j\tan\delta_j}{Z_j-iZ(j+1)\tan\delta_j} \tag{1}$$

where $Z(j)$ is the wave impedance at interface j (represented as I, II, III and IV in Figure 1(a)) between two layers, Z_j is the characteristic impedance of layer j and δ_j is the phase shift in layer j.

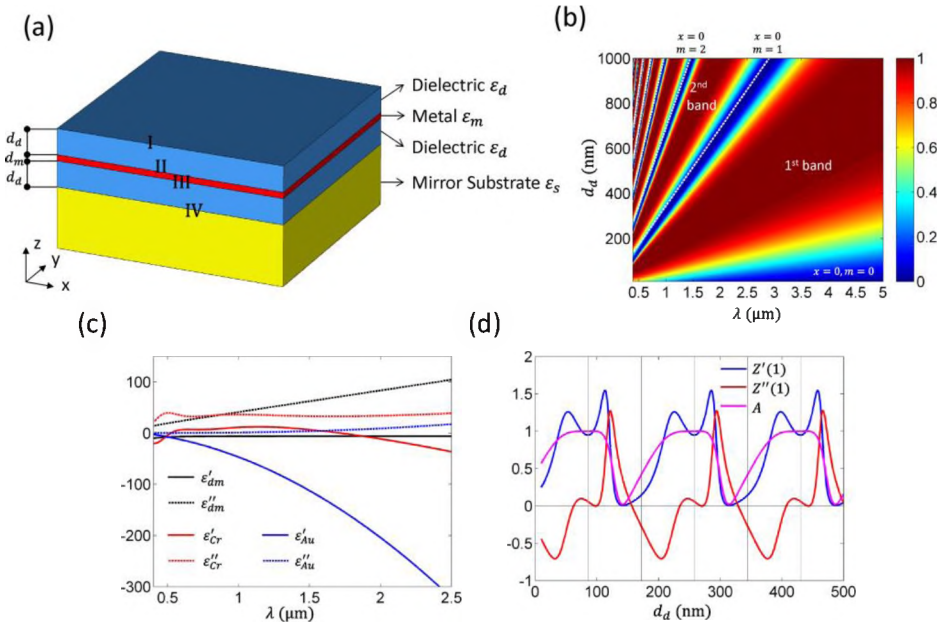

Figure 1. Design of the 3-layer absorber. (a) Schematic of a 3-layer absorber consisting of two dielectric layers (with permittivity of ε_d and thickness of d_d), one metal layer (with permittivity of ε_m and thickness of d_m) in the middle and a mirror substrate (with permittivity of ε_s and a large thickness of 200 nm to eliminate transmission, $T=0$) made of gold. The impedance at interface I, II, III and IV can be calculated from bottom to top step by step according to the impedance transformation method. (b) Theoretically calculated absorption of the 3-layer absorber based on the desired metal permittivity as a function of wavelength λ and dielectric thickness d_d. The white dashed lines represent the beginning of each absorption band where $x=0$, $m=0,1,2\ldots$, and the first band is between $m=0$ and $m=1$, and the second band is between $m=1$ and $m=2$, etc.. (c) Permittivity of each metal. Black lines are for the designed matched metal, red lines are for Cr and blue lines are for Au. (d) Impedance and absorption bands at $\lambda=500\ nm$ of the 3-layer absorber based on the desired metal permittivity when the dielectric thickness d_d is tuned. The dark gray lines represent the end of each band ($x=0$) and the bright gray lines represent the middle of each band ($x=\infty$).

In this way, the wave impedance at any interface can be derived step by step by imaging a reference plane going from bottom to top and finally achieve the ultimate wave

impedance at the top surface, $Z(1)$. Consequently, since $Z(1)$ is the impedance for the entire structure, the ultimate reflection R of the whole structure can be calculated by:

$$R = \left| \frac{Z(1) - Z_0}{Z(1) + Z_0} \right|^2 \tag{2}$$

where Z_0 is the impedance of the free space. As indicated in this equation, with the impedance match condition, $Z(1) = Z_0$, reflection can be zero leading to perfect absorption. The purpose of this proposed design is to make the impedance of the whole structure approach the free space impedance and thus obtain high or even perfect absorption by selecting materials and optimizing thicknesses for both the dielectric and metal layers.

For the 3-layer structure described in Figure 1(a), under normal incidence, its wave impedance for the entire structure can be explicitly written as:

$$Z(1) = \frac{N_m \tan^2(D)\left[n_d^2 - iN_{Au}N_m \tan(M)\right] + n_d \tan(D)\left[2iN_{Au}N_m + \left(n_d^2 + N_m^2\right)\tan(M)\right] - n_d^2\left[N_m - iN_{Au}\tan(M)\right]}{n_d \tan^2(D)\left[N_{Au}n_d N_m - in_d^3 \tan(M)\right] + n_d \tan(D)\left[2in_d^2 N_m + N_{Au}\left(n_d^2 + N_m^2\right)\tan(M)\right] + n_d^2 N_m\left[-N_{Au} + iN_m \tan(M)\right]} \tag{3}$$

where N_m is the complex refractive index of the metal, n_d is the real part of the refractive index of the dielectric since the imaginary part is almost zero for dielectrics, N_{Au} is the complex refractive index of the substrate made of Au and M and D represent the phase shift in the metal layer and the dielectric layer, respectively. Here, M is equal to $\kappa_0 N_m d_m$, and D is equal to $\kappa_0 n_d d_d$ where κ_0 is the wave number of the incident wave in vacuum. To simplify and further analyze Eq. 3, two assumptions are made: first, the metal layer is very thin compared with the incident light wavelength, $\delta_m = \kappa_0 d_m \ll 1$, resulting in $\tan(M) \approx M$; second, since the real part of gold refractive index is close to zero in the visible and near infrared (NIR) range, N_{Au} only contains the imaginary part and can be written as $N_{Au} = ik_{Au}$. Meanwhile, it is also noticed that permittivity is defined

as refractive index squared, $\varepsilon_d = n_d^2$ and $\varepsilon_m = N_m^2$. Under these conditions, Eq. 3 can be finally simplified and rewritten as:

$$Z(1) = i\frac{A_1 + A_2\varepsilon_m}{B_1 + B_2\varepsilon_m} \tag{4}$$

where

$A_1 = \varepsilon_d \tan^2(D) + n_d\left[-2k_{Au} + \varepsilon_d\delta_m\right]\tan(D) - \varepsilon_d\left[k_{Au}\delta_m + 1\right]$,

$A_2 = k_{Au}\delta_m \tan^2(D) + n_d\delta_m \tan(D)$,

$B_1 = -\varepsilon_d\left[k_{Au} - \varepsilon_d\delta_m\right]\tan^2(D) - n_d\left[2\varepsilon_d + \varepsilon_d k_{Au}\delta_m\right]\tan(D) + \varepsilon_d k_{Au}$,

$B_2 = -n_d k_{Au}\delta_m \tan(D) - \varepsilon_d\delta_m$.

It is obvious that A_1, A_2, B_1 and B_2 are all real numbers, while only ε_m includes both the real and imaginary parts, $\varepsilon_m = \varepsilon_m^{'} + i\varepsilon_m^{''}$, resulting in a complex number of the impedance, $Z(1) = Z'(1) + iZ''(1)$. By multiplying the conjugate of the denominator of Eq. 4, $Z(1)$ can be rearranged as:

$$Z(1) = Z'(1) + iZ''(1) = \frac{f_R + if_I}{f_D} \tag{5}$$

where $f_R = \varepsilon_m^{''}\left(A_1B_2 - A_2B_1\right)$, $f_I = \left(A_1 + A_2\varepsilon_m^{'}\right)\left(B_1 + B_2\varepsilon_m^{'}\right) + A_2B_2\varepsilon_m^{''2}$ and $f_D = \left(B_1 + B_2\varepsilon_m^{'}\right)^2 + \left(B_2\varepsilon_m^{''}\right)^2$.

It is easy to know that f_D is always positive, and accordingly the sign of $Z'(1)$ will be determined by the sign of f_R. After factorizing f_R, it can be seen that f_R can be also treated as a positive number because the two roots for f_R, $x_{fR1} = -\frac{n_d}{k_{Au}}$ and $x_{fR2} = -\frac{n_d + k_{Au}n_d\delta_m}{k_{Au} - \varepsilon_d\delta_m}$, are actually very close to each other, and f_R can be rewritten as:

$$f_R \approx P_R\left(x^2+1\right)\left(x+\frac{n_d}{k_{Au}}\right)^2 \geq 0 \tag{6}$$

where $x=\tan(D)$, and $P_R=\varepsilon_m'' k_{Au}\varepsilon_d\delta_m\left(k_{Au}-\varepsilon_d\delta_m\right)$ is always positive due to $\delta_m \ll 1$. However, different from the real part of $Z(1)$, its imaginary part $Z''(1)$ can be positive or negative. As a consequence, these conclusions guarantee the possibility to get the impedance match conditions that $Z'(1)$ is positive and close to 1, $Z'(1)\to 1$, and $Z''(1)$ can be positive or negative but close to 0, $Z''(1)\to 0^{\pm}$. Actually, in general, negative impedance cannot be achieved without extra energy injected into the system, but Eq. 5 still leads to such a conclusion mathematically which will make the discussion on the impedance match conditions easier.

At the same time, Eq. 4 implies that the impedance will be changed periodically as the incident wavelength λ_0 or the dielectric thickness d_d varies since the impedance is a function of $\tan(D)$ which is a periodic function of D. As a result, the absorption would also be periodically altered with λ_0 and d_d, corresponding to different absorption bands as shown in Figure 1(b). In this figure, the absorption is calculated as a function of λ_0 and d_d with SiO_2 as the dielectric and the desired metal permittivity ε_{dm} as the metal permittivity which will be discussed later. Specifically, the beginning of each absorption band and the middle of each band are corresponding to $x=0$ and $x=\infty$, respectively, and the corresponding dielectric thickness can be calculated as:

$$\begin{aligned} x=0:\ d_d &= \frac{m}{2n_d}\lambda_0, \qquad m=0,1,2,\ldots; \\ x=\infty:\ d_d &= \frac{(m+0.5)}{2n_d}\lambda_0, \qquad m=0,1,2,\ldots \end{aligned} \tag{7}$$

If the dielectric thickness d_d is fixed, absorption will be changed periodically with the wavelength λ_0; on the other hand, if the wavelength λ_0 is fixed, absorption will

be changed periodically with the dielectric thickness d_d. Accordingly, the bandwidth of each absorption band is determined by the ratio between d_d and λ_0, which is relevant to the dielectric refractive index n_d and the band order m. Particularly, for the first absorption band, the absorption range in wavelength is only determined by n_d when the 3-layer absorber is made with a proper dielectric thickness. And when n_d becomes smaller, the absorption range gets broader. Therefore, SiO_2 is selected as the dielectric due to its relatively small refractive index ($n_{SiO_2} = 1.45$).

In view of selecting a material for the metal, ε_m in Eq. 4 is discussed and a designed permittivity of the metal ε_{dm} is given out to make the absorption highest and broadest at the same time. First of all, the beginning of each absorption band is considered. When $x = 0$ is substituted into Eq. 4, the impedance would be:

$$Z(1) = i\frac{k_{Au}\delta_m + 1}{\delta_m\left(\varepsilon_m^{'} + i\varepsilon_m^{''}\right) - k_{Au}} \tag{8}$$

Since $\delta_m \ll 1$, it results in $Z(1) \to 0 - i/k_{Au}$, which means that the real part of $Z(1)$ is zero leading to complete impedance mismatch and high reflection. So the absorption at the beginning of each band is always close to zero no matter what metal is selected. It can be also understood by imaging the real case: when $x = 0$, it means that the metal layer is on the mirror substrate directly without dielectric layers, so the impedance is as metal and the reflection is very high. This conclusion can be also proved from the solutions to f_R, $x_{fR} = -\frac{n_d}{k_{Au}}$,as discussed previously. Since $-\frac{n_d}{k_{Au}}$ is close to zero, it implies that when x is close to zero, the real part of the impedance will approach zero.

Secondly, the middle of each absorption band is taken into account. For the purpose to make each absorption band broadest and highest simultaneously, the impedance at the middle of each band should be matched with the free space impedance. On one hand, the impedance is continuous and with no pole in the whole range since f_D

is always positive. On the other hand, it is already known that absorption is always close to zero at the beginning of each band. In consequence, the broadest absorption range covers the full band without break by making the impedance at the middle of each band perfectly matched with the free space impedance. In particular, at the middle of each absorption band, x is equal to infinite, and the impedance can be obtained as:

$$Z(1)=\frac{k_{Au}\delta_m\varepsilon_m^{''}-i\left(\varepsilon_d+k_{Au}\delta_m\varepsilon_m^{'}\right)}{\varepsilon_d\left(k_{Au}-\varepsilon_d\delta_m\right)} \tag{9}$$

Eq. 9 indicates that at the middle of each absorption band, the real part of the impedance is a function of the imaginary part of the metal permittivity only, $Z(1)^{'}\sim f\left(\varepsilon_m^{''}\right)$; while the imaginary part of the impedance is a function of the real part of the metal permittivity only, $Z(1)^{''}\sim f\left(\varepsilon_m^{'}\right)$. This conclusion makes designing the metal permittivity very convenient since the real part and the imaginary part can be achieved independently. To make the impedance perfectly matched with the free space impedance, $Z(1)=Z_0=1+i0$, the desired metal permittivity can be given out as:

$$\varepsilon_m^{'}(\lambda)=-\frac{\varepsilon_d}{k_{Au}\delta_m},\ \varepsilon_m^{''}(\lambda)=\frac{\varepsilon_d\left(k_{Au}-\varepsilon_d\delta_m\right)}{k_{Au}\delta_m} \tag{10}$$

Moreover, it is noticed that the desired metal permittivity is a function of the wavelength since δ_m is a function of the wavelength and the gold refractive index is also relevant to the wavelength. The desired metal permittivity is plotted out as shown in Figure 1(c), and it can be seen that $\varepsilon_m^{'}$ is close to zero compared with $\varepsilon_m^{''}$ and almost a constant, while $\varepsilon_m^{''}$ is relatively high and almost linearly increased with the wavelength. Especially, the absorption bands based on the desired metal permittivity is shown in Figure 1(d) when the incident wave is $500\,\mathrm{nm}$ and dielectric thickness is tuned. As mentioned, the absorption band is broadest with the perfect impedance match at the middle of each band. In reality, among the natural metal materials, it is found that the

permittivity of the refractory metal, Cr [32-34], is closest to the desired metal permittivity in the visible and NIR range with the real part close to zero and the imaginary part relatively high compared with noble metals (e.g. Au and Ag [32]) as shown in Figure 1(c). For this reason, a 3-layer absorber made of Cr is fabricated and the broadband absorption is demonstrated experimentally which will be discussed in details in the following section. In addition, the metal layer material is not limited to Cr, but also some other refractory metals and even some other high loss materials. Last but not least, it should be pointed out that the analysis method is not limited to 3-layer, but can be also applied on more layers by making some modifications to the equations.

3. EXPERIMENTAL RESULTS

In order to verify the prediction made in the theory section, a 3-layer sample made of Cr is fabricated. As shown in the scanning electron microscope (SEM) images (Figure 2(a)), the absorber consists of three layers (SiO_2-Cr-SiO_2) on the Au substrate and the whole structure is deposited on a Si wafer. In details, the top and bottom SiO_2 layers have the same thickness of 85nm, and the middle Cr layer is 8nm thick. The Au substrate, acting as a mirror, is 200nm thick to avoid any transmission through it. Since the Cr layer is very thin, to show it clearly in the SEM images, a Pt layer to protect the cross section is deposited on the top before cutting the cross section using Focused Ion Beam (FIB). The SEM images reveal that each layer is deposited with high quality. And it can be also seen from the atomic force microscope (AFM) image (Figure 2(b)) that the RMS roughness of the top surface is measured as 2.04nm. Additionally, as shown in Figure 2(c), the absorption at normal incidence is achieved by measuring the reflection using both the HR550 detector to cover the visible range and FTIR to cover the NIR range. Since there is no transmission, the absorption spectrum can be directly derived from the measured reflection spectrum ($A=1-R$). The experimental absorption spectrum is in agreement with the theoretical prediction. As expected, the absorption can cover a broad range from $0.4\mu\text{m}$ to around $1.4\mu\text{m}$ with amplitude as high as 90% since the permittivity of Cr can follow the desired metal permittivity up to around $1.4\mu\text{m}$ as shown in Figure 1(c). If the absorber is made of Au instead of Cr, the absorption will drop a lot as shown in Figure 2(c).

To clarify how the broadband absorption can be achieved by the Cr absorber, its absorption as a function of the incident wavelength and the SiO_2 thickness is plotted as shown in Figure 3(a). It indicates that the absorption bands also hold the same form as the absorber made of the desired metal permittivity. However, when the wavelength is increased, the absorption will be decreased since the permittivity of Cr is off the desired metal permittivity in long wavelength. Specifically, the impedance of the Cr absorber at $\lambda = 500$ nm as a function of the dielectric thickness is also plotted out as shown in Figure 3(b) which is similar to Figure 1(d) for the absorber made of the desired metal permittivity.

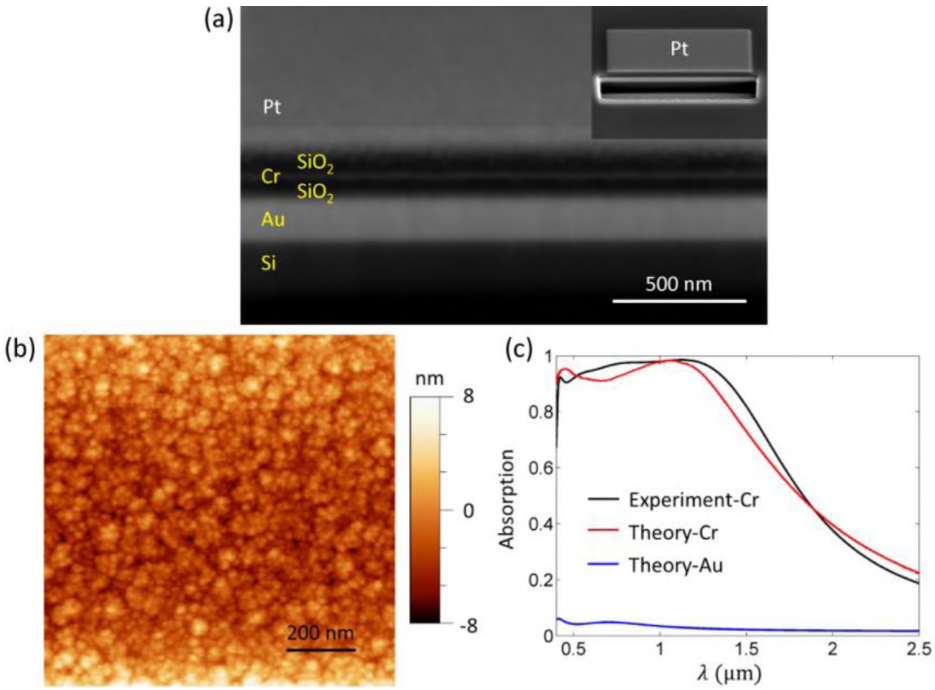

Figure 2. Experiment result of the 3-layer absorber. (a) A cross-section SEM image of the 3-layer Cr-SiO_2 absorber with a total thickness of 180 nm composed of two 85 nm thick SiO_2 layers and one 8 nm thick Cr layer. The sample is fabricated on a Si wafer and Pt is deposited on the top to protect the cross-section before cutting through the sample using Focus Ion Beam (FIB). The upper right image shows an overall view of the cross-section with a square of Pt deposited on the top. (c) A representative AFM picture showing the surface roughness distribution (the RMS roughness is 2.04 nm) for the fabricated 3-layer Cr-SiO_2 absorber. (c) Measured absorption in experiment of the 3-layer Cr-SiO_2 absorber (black curve) and its corresponding calculated absorption from theory (red curve). The blue curve is the absorption spectrum for a 3-layer Au-SiO_2 absorber which is very low over all the range.

It can be seen that $Z(1)^{'}$ (blue curve) and thus the absorption (pink curve) are always close to zero at the beginning of each absorption band (black vertical lines), while the absorption is high at the middle of each absorption band (gray vertical lines) owing to $Z(1)^{'}$ close to one and $Z(1)^{''}$ close to zero. Furthermore, this can be also elaborated from Figure 3(c) where the absorption as a function of $\varepsilon_m^{'}$ and $\varepsilon_m^{''}$ is plotted when the SiO_2 thickness is 85 nm and the incident wavelength is 500 nm. The high absorption area (red area) will go along with the desired metal permittivity (white dashed curve) as the wavelength is increased. And the permittivity of Cr (blue dashed curve) will be located in the high absorption area first and then get away from it as the wavelength is increased. However, the permittivity of Au (red dashed curve) is not located in the high absorption area at all resulting in low absorption in the whole wavelength range.

Eventually, the electric field distribution E_x under a normal incident light of 500nm plotted in Figure 3(d) proves the impedance match for the Cr absorber since the wave propagation inside the 3-layer structure remains the same form as the incident wave in the air. In another word, the 3-layer structure is viewed as air by the incident wave and there is no reflection from it. The only difference comes from the absorption inside the Cr layer with regard to the wave intensity. And this is illustrated from the time average power flow $\vec{P}$ (black arrows) in Figure 3(d) which keeps the same intensity in the air and in the top SiO_2 layer but decays fast after the Cr layer. Since the normalized time average energy density $|W|$is mainly confined inside the metal layer as shown in Figure 3(e), the heat generation density distribution is mostly located inside the Cr layer rather than the Au substrate as shown in Figure 3(f). This also demonstrates that the Au substrate just plays a role as mirror to reflect light back and eliminate transmission.

Optical measurements for absorption spectra at different incident angles were conducted on a self-designed optical setup equipped with a white light source and the iHR550 detector. Reflection of the absorber sample can be measured over a wide spectral range from 400 nm to 1050 nm at angles of $0-80$ degrees. In Figure 4, the experimental absorption spectra at different incident angles are reported as well as the

same quantities predicted by the aforementioned theory for comparison. The absorption with incident angles can be simply calculated by adding a $\cos\theta$ coefficient to Eq. 1.

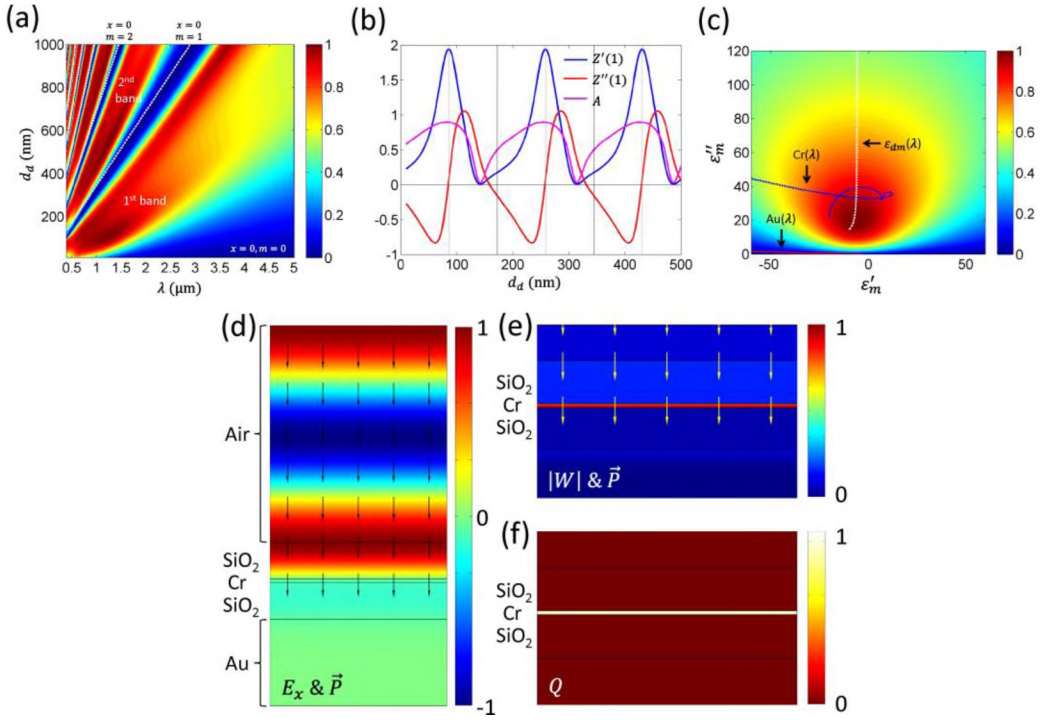

Figure 3. Simulation results of the 3-layer absorber. (a) Theoretically calculated absorption of the 3-layer Cr-SiO_2 absorber as a function of wavelength λ and dielectric thickness d_d when the metal layer thickness is $10\,\text{nm}$. (b) Impedance and absorption bands at $\lambda = 500\text{nm}$ of the 3-layer Cr-SiO_2 absorber when the dielectric thickness d_d is tuned. (c) Absorption of a 3-layer absorber as a function of the real and imaginary part of the metal permittivity ($\varepsilon_m^{'}$, $\varepsilon_m^{''}$) when $d_d = 85\,\text{nm}$ and $d_m = 8\,\text{nm}$ at $\lambda = 500\,\text{nm}$. (d), (e) and (f) are electric field distribution E_x and time average power flow $\vec{P}$ (black arrows), normalized time average energy density $|W|$ and heat generation density distribution Q under a normal incident light of $500\,\text{nm}$, respectively.

It can be seen that the experimental absorption spectra are in high agreement with the theoretical predictions except for some high angle (close to 80 degree) results due to measurement errors and fabrication defects. As predicted in the theory, the broadband absorber is insensitive to the incident angle (the absorption is still over 80% up to 70 degree). In addition, the angular absorption spectra include two polarizations (TE as shown in Figure 4(a-b) and TM as shown in Figure 4 (c-d)). The TE and TM spectra are the same under normal incidence and similar at low incident angles, but become different

at high incident angles. A dip is found in the TM spectra around 450 nm but there is a peak around 450nm for TE. In brief, since the absorption is kept at a high level over a large incident angle range for both TE and TM, the broadband absorber is angle-insensitive, polarization-insensitive and omnidirectional.

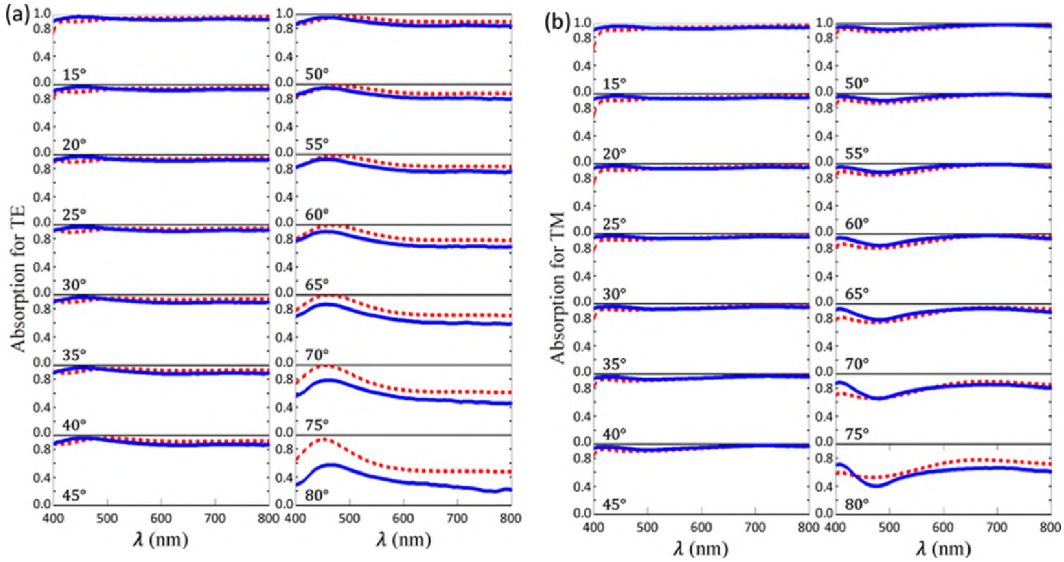

Figure 4. The measured absorption spectra (solid blue curves) and the calculated absorption spectra (dashed red curves) in the wavelength range of $400-800$ nm at different incident angles ($15-80$ degrees) for (a) TE polarization and (b) TM polarization measured absorption (right panel) and calculated absorption (left panel) in the range of $400\sim1050$nm under different angles and different polarizations (TE & TM).

4. DISCUSSION

As mentioned in the theory session, the absorption can be further improved by adding more layers to the current 3-layer design. As shown in Figure 5(a), for a 5-layer absorber made of Cr and SiO_2 alternatively, the absorption can reach over 2um if the SiO_2 thickness is proper. This is because the order of the equations will be increased leading to solutions in a broader range. Another way to expand the absorption bandwidth is to decrease the metal thickness as shown in Figure 5(b) where the absorption bandwidth can go up to 3um when the Cr thickness is reduced to 5nm. The reason is that although the metal thickness is just reduced with several nanometers, the reducing percentage is significant since the original metal thickness itself is small and this will

result in a better approach to the assumption of $\delta_m \ll 1$. Hence, the impedance can be better matched, and it will give more tolerance for the Cr permittivity getting away from the desired metal permittivity in long wavelength.

Once again, selecting a proper material matched with the desired metal permittivity is critical for improving the absorption. It is possible to utilize an artificial metamaterial (e.g. multilayer structure or nanowire structure made of different metals and dielectrics) replacing the current metal layer to make the absorption broader. Although it might increase the metal layer thickness, some modifications to the derived equations can be made to regain the impedance match conditions. Similarly, some oxide materials with doping, like Indium tin oxide (ITO) are also able to be used in the broadband absorber design because of their high loss. If so, the thickness of both the metal layer and the dielectric layer should be tuned to compensate the impedance match conditions.

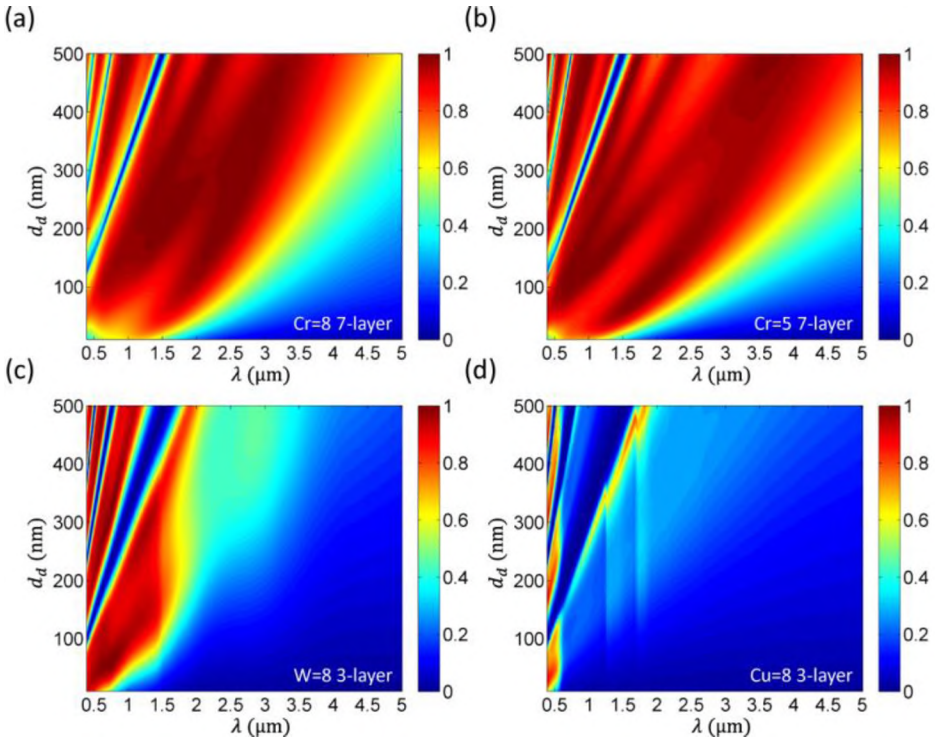

Figure 5. Calculated absorption as a function of wavelength and dielectric thickness d_d for different absorbers made of different layer numbers, different metal layer thickness or different metals. (a) is for a 7-layer absorber made of 8 nm thick Cr, (b) is for a 7-layer absorber made of 5 nm thick Cr, (c) is for a 3-layer absorber made of 8 nm thick W and (d) is for a 3-layer absorber made of 8 nm thick Cu.

Furthermore, refractory metals are better than noble metals for the proposed broadband absorber. To show how other metals work in the broadband absorber compared with Cr, absorptions for different metals are calculated as a function of wavelength λ and dielectric thickness d_D at normal incidence. As shown in Figure 5(c), the absorber made of another refractory metal W is similar but not as good as Cr with its absorption band reaching $1.4\,\mu m$ and declining suddenly beyond $1.4\,\mu m$. On the contrary, absorbers made of noble metals are not as good as the refractory metal absorbers. As shown in Figure 5(d), the absorption for Cu cannot be increased to a high level after 0.5um no matter what the dielectric thickness is.

Finally, since refractory metals are extraordinarily resistant to heat and with high melting points, the proposed broadband absorber made of refractory metal can also act as broadband emitter working at high temperature. For instance, the melting point of bulk Cr is $2180\,K$ resulting in a peak wavelength of $1.33\,\mu m$ for blackbody radiation. And the melting point of bulk W is even higher, $3695\,K$, resulting in a peak wavelength of $0.784\,\mu m$. However, the melting point of bulk Au is just $1337\,K$ leading to a peak wavelength of $2.17\,\mu m$. Although the melting points for metals in nanoscale would be below their bulk melting points due to size effect [36], refractory metals still hold higher melting points than noble metals. Therefore, emitters made of refractory metal possibly work at a relatively high temperature to emit light in visible range or NIR range.

5. CONCLUSIONS

In conclusion, an ultrathin 3-layer broadband absorber made of the refractory metal Cr without patterning is presented. In theory, the broadband absorption is analyzed based on the impedance transformation method and the desired metal permittivity is derived to guide the design for the optimal absorption. There are three deduced conditions in the analysis: firstly, the real part of the impedance is proved to be positive mathematically resulting in the possibility of achieving the impedance match conditions ($Z'(1) \to 1$ and $Z''(1) \to 0$); secondly, the beginning of each absorption band is found to be close to zero since the real part of the impedance is almost zero at the beginning of each band; finally, the impedance at the middle of each absorption band should be matched with the free space impedance to make the absorption broadest and highest

simultaneously since the impedance is continuous and without pole in all the range. Meanwhile, it is found that the permittivity of refractory metals is closest to the desired metal permittivity in the visible and NIR range making the absorption up to 1.4 um. Thus, in experiment, the 3-layer Cr-SiO_2 absorber is fabricated. And its absorption can cover the range of 0.4-1.4 um with amplitude over 90%. The absorption at different incident angles and with TE/TM polarizations are also measured, and it turns out that the broadband absorber is angle-insensitive, polarization-insensitive and omnidirectional.

Additionally, the current design can be further improved in several ways. On one hand, by following the desired metal permittivity, the metal layer can be filled with some artificial metamaterials or doped oxide materials. On the other hand, although it is realized that refractory metals are better than noble metals or other metals, the absorption for absorbers made of refractory metals can be also improved by adding more layers and reducing the metal layer thickness. Finally, refractory metals are not only good for broadband absorption, but also for emission because they can work at high temperature due to the high melting point. With all the features, the demonstrated ultrathin 3-layer broadband absorber can be used in many exciting applications, such as solar energy harvesting systems, thermo-photovoltaic energy conversion devices, thermal imaging and emissivity control.

ACKNOWLEDGEMENT

The authors acknowledge the support from the Ralph E. Powe Junior Faculty Enhancement Award and the National Science Foundation under grant CBET-1402743. This work was performed, in part, at the Center for Nanoscale Materials, a U.S. Department of Energy, Office of Science, Office of Basic Energy Sciences User Facility under Contract No. DE-AC02-06CH11357.

REFERENCES

[1] Y. Cui, Y. He, Y. Jin, F. Ding, L. Yang, Y. Ye, S. Zhong, Y. Lin, and S. He, "Plasmonic and metamaterial structures as electromagnetic absorbers," Laser & Photon. Rev. 8, 495—520 (2014).

[2] C. M. Watts, X. Liu, and W. J. Padilla, "Metamaterial Electromagnetic Wave Absorbers," Adv. Mater. 24, OP98—OP120 (2012).

[3] T. V. Teperik, F. J. Garcia de Abajo, A. G. Borisov, M. Abdelsalam, P. N. Bartlett, Y. Sugawara, and J. J. Baumberg, "Omnidirectional absorption in nanostructured metal surfaces," Nat. Photonics 2, 299—301 (2008).

[4] S. Molesky, C. J. Dewalt, and Z. Jacob, "High temperature epsilon-near-zero and epsilon-near-pole metamaterial emitters for thermophotovoltaics," Opt. Express 21, A96—A110 (2013).

[5] C. Wu, B. Neuner III, J. John, A. Milder, B. Zollars, S. Savoy and G. Shvets, "Metamaterial-based integrated plasmonic absorber/emitter for solar thermo-photovoltaic systems," J. Opt. 14, 024005 (2012).

[6] H. Deng, T. Wang, J. Gao, and X. Yang, "Metamaterial thermal emitters based on nanowire cavities for high-efficiency thermophotovoltaics," J. Opt. 16, 035102 (2014).

[7] N. I. Landy, C. M. Bingham, T. Tyler, N. Jokerst, D. R. Smith, and W. J. Padilla, "Design, theory, and measurement of a polarization-insensitive absorber for terahertz imaging," Phys. Rev. B 79, 125104 (2009).

[8] X. Liu, T. Tyler, T. Starr, A. F. Starr, N. M. Jokerst, and W. J. Padilla, "Taming the Blackbody with Infrared Metamaterials as Selective Thermal Emitters," Phys. Rev. Lett. 107, 045901 (2011).

[9] B. J. Lee, and Z. M. Zhang, "Design and fabrication of planar multilayer structures with coherent thermal emission characteristics," J. Appl. Phys. 100, 063529 (2006).

[10] K. Aydin, V. E. Ferry, R. M. Briggs, and H. A. Atwater, "Broadband polarization-independent resonant light absorption using ultrathin plasmonic super absorbers," Nat. Commun. 2, 517 (2011).

[11] Y. Q. Ye, Y. Jin, and S. He, "Omnidirectional, polarization-insensitive and broadband thin absorber in the terahertz regime," J. Opt. Soc. Am. B 27, 498—504 (2010).

[12] W. Wang, Y. Cui, Y. He, Y. Hao, Y. Lin, X. Tian, T. Ji, and S. He, "Efficient multiband absorber based on one-dimensional periodic metal–dielectric photonic crystal with a reflective substrate," Opt. Lett. 39, 331—334 (2014).

[13] J. Yu, Y. Shen, X. Liu, R. Fu, J. Zi and Z. Zhu, "Absorption in one-dimensional metallic–dielectric photonic crystals," J. Phys.: Condens. Matter 16, L51—L56 (2004).

[14] N. Mattiucci, M. J. Bloemer, N. Akozbek, and G. D'Aguanno, "Impedance matched thin metamaterials make metals absorbing," Sci. Rep. 3, 3203 (2013).

[15] Y. Cui, K. H. Fung, J. Xu, H. Ma, Y. Jin, S. He, and N. X. Fang, "Ultrabroadband Light Absorption by a Sawtooth Anisotropic Metamaterial Slab," Nano Lett. 12, 1443—1447 (2012).

[16] J. Zhou, A. F. Kaplan, L. Chen, and L. J. Guo, "Experiment and Theory of the Broadband Absorption by a Tapered Hyperbolic Metamaterial Array," ACS Photonics 1, 618—624 (2014).

[17] D. Ji, H. Song, X. Zeng, H. Hu, K. Liu, N. Zhang, and Q. Gan, "Broadband absorption engineering of hyperbolic metafilm patterns," Sci. Rep. 4, 4498 (2014).

[18] H. A. Haus, Waves and fields in optoelectronics (Prentice-Hall, Inc., 1984).

[19] E. D. Palik, Handbook of Optical Constants of Solids (Academic Press, 1998).

[20] D. Barchiesi, and T. Grosges, "Fitting the optical constants of gold, silver, chromium, titanium, and aluminum in the visible bandwidth," J. Nanophotonics 8, 083097 (2014).

[21] A. D. Rakic, A. B. Djurišić, J. M. Elazar, and M. L. Majewski, "Optical Properties of Metallic Films for Vertical-Cavity Optoelectronic Devices," Appl. Opt. 37, 5271—5283 (1998).

[22] W. Woltersdorff, "Über die optischen Konstanten dünner Metallschichten im langwelligen Ultrarot," Z. Phys. 91, 230—252 (1934).

[23] S.-A. Biehs, D. Reddig, M. Holthaus, "Thermal radiation and near-field energy density of thin metallic films," Eur. Phys. J. B 55, 237—251 (2007).

[24] P. Buffat, and J. P. Borel, "Size effect on the melting temperature of gold particles," Phys. Rev. A 13, 2287—2298 (1976).

III. BROADBAND INFRARED ABSORBERS WITH STACKED DOUBLE CHROMIUM RING RESONATORS

Huixu Deng, Liliana Stan, David A. Czaplewski, Jie Gao, and Xiaodong Yang

Department of Mechanical and Aerospace Engineering

Missouri University of Science and Technology, Rolla, Missouri 65409, U.S.A.

ABSTRACT

A broadband absorber in the infrared wavelength range from 1 μm up to 5 μm is designed and demonstrated with stacked double chromium ring resonators on a reflective chromium mirror. The near-perfect broadband absorption is realized by combining the multilayer impedance match in the short wavelength range and the double plasmonic resonances in the long wavelength range, which is illustrated with an equivalent circuit model for the impedance analysis. The broadband absorber is proved to be angle-insensitive and polarization-independent due to the geometrical symmetry. The thermal analysis for heat generation and temperature distributions inside the absorber structure is also investigated.

Keywords: Absorption, Resonance, Infrared, Metamaterials

1. INTRODUCTION

Broadband infrared absorbers have been widely studied recently [1,2] due to their crucial roles in various applications such as solar energy harvesting [3,4], thermophotovoltaic energy conversion [5–7], thermal emission [8,9], thermal imaging [10], and stealth devices [11]. Diverse methods have been considered to obtain broadband absorption based on different mechanisms including the combination of multiple resonances in metasurfaces [4,8,12], exciting interferences in metal-dielectric stacks [3,13–15], achieving impedance match in multilayers with free space [16,17], and the generation of slow light in tapered multilayer waveguides [18–21].

In this paper, a broadband infrared absorber made of stacked double chromium (Cr) ring resonators on a chromium mirror is designed based on the combination of

multilayer impedance match in the short wavelength range and the double plasmonic resonances in the long wavelength range. The absorber structure is milled from two pairs of Cr-SiO_2 layers with overall thickness of 360 nm on a reflective substrate. Different from combining multiple resonators in the same horizontal plane, the proposed absorber has double Cr ring resonators stacked in the vertical direction. At the same time, the stacked double ring structure can be effectively regarded as one-dimensional metal-dielectric multilayer lattice for satisfying impedance match conditions in the short wavelength range. An equivalent circuit (EC) model is developed to analyze and optimize the broadband absorber according to the transmission line theory for the multilayer impedance in the short wavelength range and the coupled lumped-element LC resonators [22–25] for the resonance impedance in the long wavelength range. The absorption spectra predicted by the EC model agree with both the simulated and measured absorption spectra and can explain the two absorption mechanisms thoroughly. Further investigations on the oblique incidence under different polarizations, resonant mode fields, heat generation and temperature increase are also performed.

2. ABSORBER DESIGN AND EQUIVALENT CIRCUIT MODEL

The designed infrared absorber is based on a multilayer stack consisting of two pairs of Cr-SiO_2 layers with 30 nm thick Cr and 150 nm thick SiO_2 in each pair deposited on top of a 200 nm thick Cr mirror coated on a silicon wafer. There is an additional 30 nm thick SiO_2 protecting layer deposited on top of the multilayer stack to prevent the top Cr layer from oxidation. The multilayer stack is grown by RF sputtering. The Cr is grown in an Ar atmosphere at 5 mTorr pressure at a deposition rate of $0.5\ \text{Å/sec}$ and the SiO_2 is grown in a 12:1 mixture of Ar:O_2 at a rate of $0.14\ \text{Å/sec}$. Figure 1(a) shows a scanning electron microscope (SEM) image of the deposited Cr-SiO_2 multilayer before milling where each layer can be clearly seen. The thick Cr mirror will block any transmission through the sample. At first, the absorption spectrum of the multilayer film is measured using Fourier transform infrared spectroscopy (FTIR). As shown in Figure 1(b), the experimental absorption is below 50% in the range of $1 \sim 5\ \mu\text{m}$, which can be matched well with simulation (COMSOL Multiphysics software), by using the Cr permittivity of

$\varepsilon_{Cr} = \varepsilon_{Cr}^{'} + i\varepsilon_{Cr}^{''}$ shown in Figure 1(c) calculated according to the Brendel-Bormann model [26–28]. The SiO_2 permittivity is equal to a constant $\varepsilon_{SiO_2} = 2.25$.

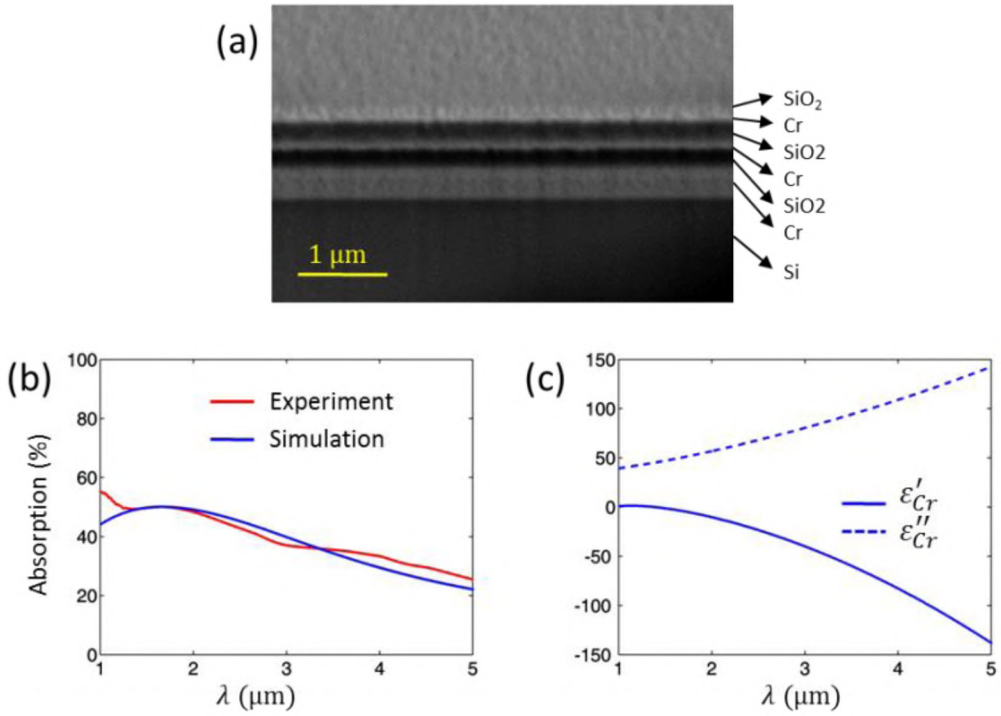

Figure 1. Experiment spectra of the multilayer (a) SEM image of the Cr-SiO_2 multilayer film before milling. (b) Absorption spectra of the multilayer film from both experiment (red curve) and simulation (blue curve). (c) The real (solid curve) and imaginary (dashed curve) parts of Cr permittivity.

The schematic of the designed absorber with stacked double ring resonators is illustrated in Figure 2(a). The absorber structure is fabricated using Focused Ion Beam (FIB) milling in two steps. First, the top pair of Cr-SiO_2 layer is milled to form the top ring resonator; and then the bottom pair of Cr-SiO_2 layer is milled to form the bottom ring resonator. During the FIB milling, a SiO_2 layer with very thin thickness is remained on top of the second Cr layer to avoid oxidation. Due to the zero transmission from the absorber, the absorption A is merely determined by the reflection R and is equal to $A = 1 - R$. The Cr layers have the thickness of $t_m = 30\,\text{nm}$ and the two SiO_2 layers have the thickness of $t_d = 150\,\text{nm}$. In one unit cell, the period in x and y directions are both equal to P. For one design, when the period is $P = 700\,\text{nm}$, the top ring width is

$w_t = 350\text{nm}$ and the bottom ring width is $w_b = 600\text{nm}$. The inner hole size of the two rings is the same with $w_i = 175\text{nm}$.

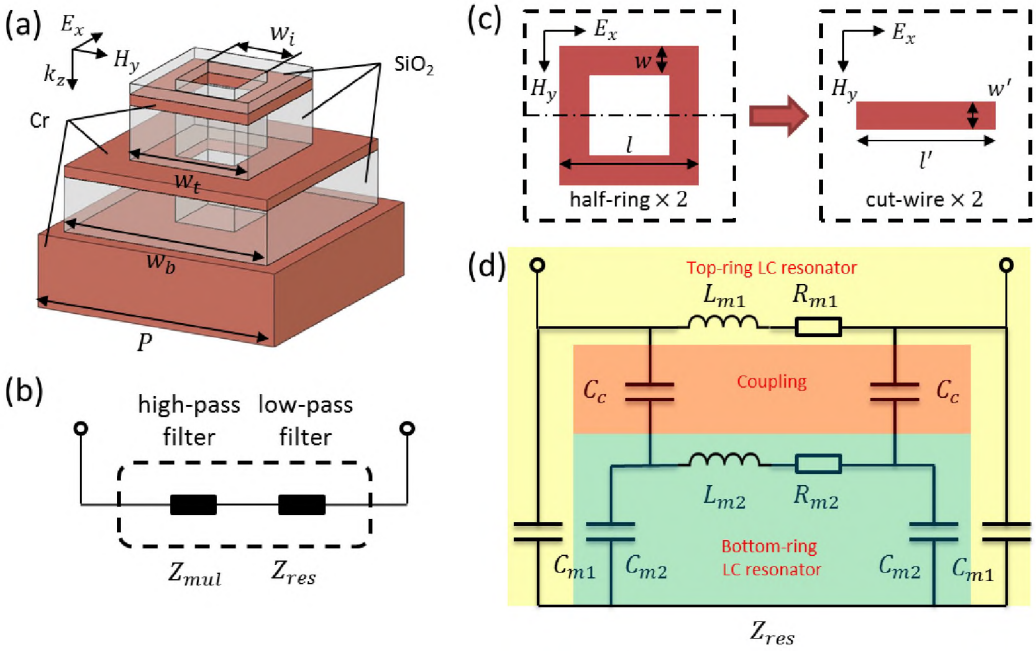

Figure 2. Design of the stacked double ring absorber. (a) Schematic of the designed broadband infrared absorber consisting of stacked double Cr ring resonators milled from two pairs of Cr-SiO_2 layers on top of a reflective Cr mirror. (b) Equivalent circuit model of the total impedance for the double-ring absorber consisting of Z_{mul} as a high-pass filter and Z_{res} as a low-pass filter. (c) Transformation of two half-rings of width w and length l into two equal cut-wires of effective width w' and effective length l'. (d) Equivalent circuit for Z_{res} based on the coupled lumped-element LC resonators.

An equivalent circuit (EC) model is developed to evaluate the broadband absorption mechanism of the designed double-ring absorber by considering the combination of the multilayer impedance match in the short wavelength range and the double plasmonic resonances in the long wavelength range. The multilayer impedance Z_{mul} can be regarded as a high-pass filter with no reflection at high frequencies and the resonance impedance Z_{res} can be treated as a low-pass filter with no reflection at low frequencies. As shown in Figure 2(b), the EC model is then built up by adding the two impedances together in series to estimate the total impedance of the absorber,

$Z_{tot} = Z_{mul} + Z_{res}$. And the absorption can be calculated as $A = 1 - \left((Z_{tot} - Z_0)/(Z_{tot} + Z_0)\right)^2$, where Z_0 is the impedance of free space.

Z_{mul} can be evaluated according to the transmission line theory by regarding the double-ring resonators as effective one-dimensional metal-dielectric multilayer lattice in the vertical direction [17,29,30],

$$Z_{mul} = Z(1), \text{ and } Z(j) = \frac{Z_j\left(Z(j+1) - iZ_j \tan\delta_j\right)}{Z_j - iZ(j+1)\tan\delta_j}, j = 1,2,...,6 \quad (1)$$

where $Z(1)$ represents the wave impedance of the whole multilayer structure seen from the top and can be calculated layer by layer starting from the bottom Cr mirror with the wave impedance of $Z(6)$ up to the top SiO_2 protecting layer with the wave impedance of $Z(1)$, by considering the phase shift δ_j and the characteristic impedance Z_j for each layer j of the multilayer lattice. $\delta_j = f_{pj}\kappa_0 N_j t_j$ in which κ_0 is the wave vector of incident wave, N_j is the complex refractive index and t_j is the layer thickness. Particularly, t_j is modified by a factor f_{pj} to represent the effective layer thickness due to the material milling.

Z_{res} is estimated based on the coupled lumped-element LC resonators. As shown in Figure 2(c), when the incident light has the field components of E_x and H_y, each ring resonator can be divided into two symmetric half-ring parts [31–33] of width w and length l by the central line and transformed into two cut-wires of effective width w' and effective length l'. Each cut-wire is a LC resonator consisting of three components: inductor L_m, resistor R_m and capacitor C_m. The capacitor C_e due to the electric resonance between two neighboring rings is ignored to simplify the circuit since the magnetic resonance is dominant in this structure [34]. Here, L_m can be expressed as the capacitance between two parallel plates separated by a distance [35], $L_m = a_m \mu_0 l t_d / w$, where μ_0 is the permeability of vacuum and a_m is a numerical factor considering the

effective length l' of the cut-wire. $R_m = c_r \rho l/(wt_m)$, where c_r is a numerical factor, and $\rho \equiv 1/\sigma = R' - i\omega L' = -1/(i\omega\varepsilon_0(\varepsilon_m - 1))$ is defined as the combination of intrinsic resistivity R' and inductivity L' [23] of the metal (with relative permittivity of ε_m) since the contribution of the drifting electrons cannot be neglected at infrared frequencies [22,24,33]. C_m is formed between the half-ring and the Cr mirror due to the magnetic resonance and evaluated by the capacitance between two parallel plates separated by the dielectric spacer [32,35], $C_m = b_m \varepsilon_0 \varepsilon_d w(0.5l)/t_d$, where ε_0 is the permittivity of vacuum, ε_d is the relative permittivity of the dielectric spacer, and b_m is a numerical factor representing the effective capacitance area.

The equivalent circuit for Z_{res} is shown in Figure 2(d) consisting of two LC resonators. The first LC resonator includes L_{m1} and R_{m1} representing the top ring and C_{m1} between the top-ring layer and the Cr mirror. The second LC resonator is similar to the first one, but it is formed by the middle ring and the Cr mirror including circuit components of L_{m2}, R_{m2} and C_{m2}. Meanwhile, when two ring resonators are placed closely, they are coupled through the capacitor $C_c = b_c \varepsilon_0 \varepsilon_d w_1 (0.5l_1)/t_d$ between the two rings separated by the dielectric spacer [36,37]. Eventually, the calculated Z_{res} can be expressed as:

$$Z_{res} = \frac{C_c + C_{m2}}{i\omega C_c C_{m2}\left(\frac{(2C_c + C_{m2})(C_{m1}C_{m2} + C_c(C_{m1} + C_{m2}))}{C_c(C_{m2}(C_{m1} + C_{m2}) + C_c(C_{m1} + 3C_{m2}))} + \frac{C_c + C_{m2}}{i\omega C_c C_{m2} R_{m1} - \omega^2 C_c C_{m2} L_{m1}} - \frac{C_c}{C_{m2}(-2 + \omega(C_c + C_{m2})(-iR_{m2} + \omega L_{m2}))}\right)} \quad (2)$$

3. DEMONSTRATION OF BROADBAND INFRARED ABSORBER

The broadband absorption response of the double-ring absorber can be evaluated by combing the two impedances of Z_{mul} and Z_{res} together. As an example, for the absorber with period of $P = 700$ nm, Figure 3(a) shows the absorption spectra calculated by the EC model and the simulation result (COMSOL Multiphysics software). In order to

fit the simulated resonance peaks of two ring resonators and absorption amplitude, the coefficients used in the EC model for the double-ring absorber with $P = 700$ nm are set as the following: $f_{pj} = 0.8, 0.17, 0.8, 0.33, 0.97$ for each effective layer of $j = 1, 2, 3, 4, 5$ respectively; $a_{m1} = 1.0$, $b_{m1} = 0.8$, $c_{r1} = 0.4$ for the top ring resonator, $a_{m2} = 1.9$, $b_{m2} = 0.75$, $c_{r2} = 0.9$ for the bottom ring resonator, and $b_c = 3.2$ for the coupling of two ring resonators. In the long wavelength range ($2 \sim 5\mu m$), the absorption is majorly due to the double ring resonances, and in the short wavelength range ($1 \sim 2\ \mu m$), the absorption is mainly due to the multilayer impedance match condition. To explain the combination of these two absorption mechanisms, Z_{mul} , Z_{res} and Z_{tot} calculated by the EC model are plotted in Figure 3(b). There are two peaks in the real part of $Z_{res} = Z_{res}^{'} + iZ_{res}^{"}$ located at about $\lambda = 2.1\mu m$ and $\lambda = 3.7\mu m$ representing the two Cr ring resonances in the long wavelength range. Correspondingly, two absorption peaks in the range of $\lambda = 2 \sim 5\mu m$ can be observed in the EC model curve in Figure 3(a). Additionally, the real part of $Z_{mul} = Z_{mul}^{'} + iZ_{mul}^{"}$ is close to $Z_0 = 1$ at about $\lambda = 1.8\mu m$ indicating that the multilayer impedance match condition can be achieved in the short wavelength range. The absorption peak of the theoretical absorption in the range of $\lambda = 1 \sim 2\mu m$ is the intersection of Z_{mul} and Z_{res} resulting from the real part of $Z_{tot} = Z_{tot}^{'} + iZ_{tot}^{"}$ close to $Z_0 = 1$.

In order to show how the absorption spectrum change with the absorber structure size, three double-ring absorbers with different periods and ring sizes are fabricated. As shown in Figures 4(a)-(c), the solid curves are the measured absorption spectra for the double-ring absorbers with periods of $P = 600$ nm (in magenta), $P = 700$ nm (in blue) and $P = 800$ nm (in red), respectively, while the ring dimensions keep the same ratios as $W_{in} = P/4$, $W_t = P/2$, $W_b = l = P - 100(\text{nm})$ (the gap between two neighboring bottom rings is always 100 nm). The dashed curves are the simulated absorption spectra. The insert in each figure is the SEM image of the fabricated double-ring absorber. The absorption spectrum range is affected by the period P and the ring length l. When P = 600nm (with ring dimensions of $w_b = 500\text{nm}, w_t = 300\text{nm}$ and $w_i = 150\text{nm}$), the

absorption spectrum range with more than 80% absorption is $\lambda = 1 \sim 3.1\mu m$. As P is increased, the absorption spectrum range gets broader, but the absorption becomes lower. For P = 800nm (with ring dimensions of $w_b = 700nm, w_t = 400nm$ and $w_i = 200nm$), the absorption spectrum range can reach $\lambda = 1 \sim 4.8\mu m$ for the absorption over 80%. The absorber with $P = 700$ nm (with ring dimensions of $w_b = 600nm, w_t = 350nm$ and $w_i = 175nm$) is the optimized result by taking account of the trade-off between absorption spectrum range and absorption amount. Its absorption spectrum range can reach $\lambda = 1 \sim 3.75\mu m$ with the absorption over 80%.

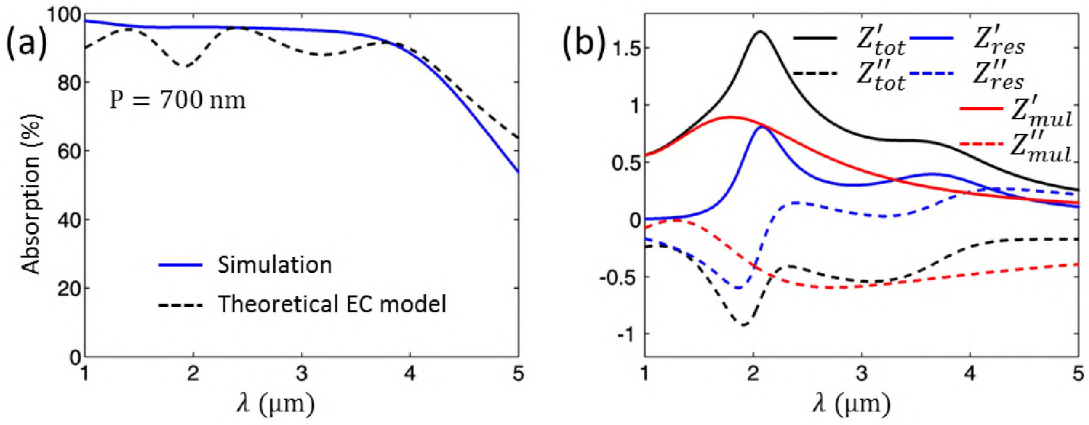

Figure 3. Theoretical result of the double ring absorber. (a) Comparison of the absorption spectra calculated from the EC model (dashed black curved) and the simulation (blue solid curve) for the double-ring absorber with $P = 700nm$. (b) The corresponding real parts (solid curves) and imaginary parts (dashed curves) of impedances for Z_{mul} (in red), Z_{res} (in blue), and Z_{tot} (in black).

The double-ring structure will change into double-square structure if the center hole has the zero width, which can make the fabrication process simpler. Similar to the double-ring structure, the double-square structure can also be regarded as two coupled plasmonic resonators. As shown in Figure 5, the double-square absorbers with the periods of $P = 600$ nm, $P = 700$ nm and $P = 800$ nm can also achieve the broadband absorption spectra with absorption above 80% similar to the double-ring absorbers. The absorption

spectrum of double-square absorber is not as flat as that of double-ring absorber, but it has a small absorption peak in the long wavelength range.

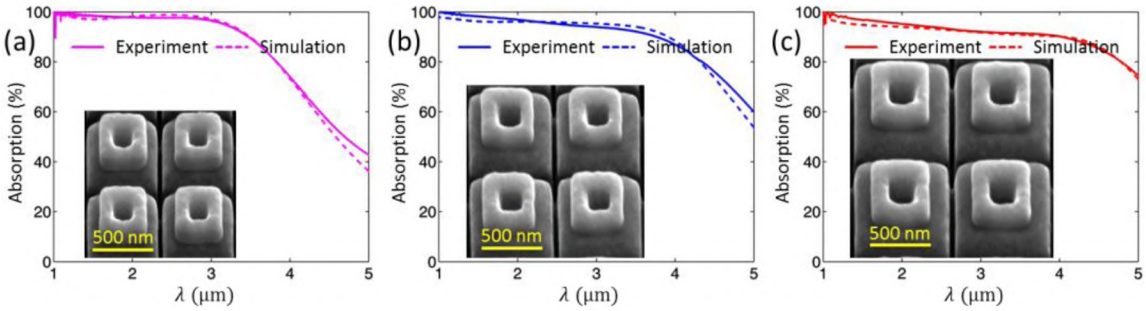

Figure 4. Experimental (solid curves) and simulated (dashed curves) absorption spectra for the double-ring absorber with (a) $P = 600\text{nm}$, (b) $P = 700\text{nm}$ and (c) $P = 800\text{nm}$, respectively. The insert is the SEM image of the fabricated double-ring absorber structure.

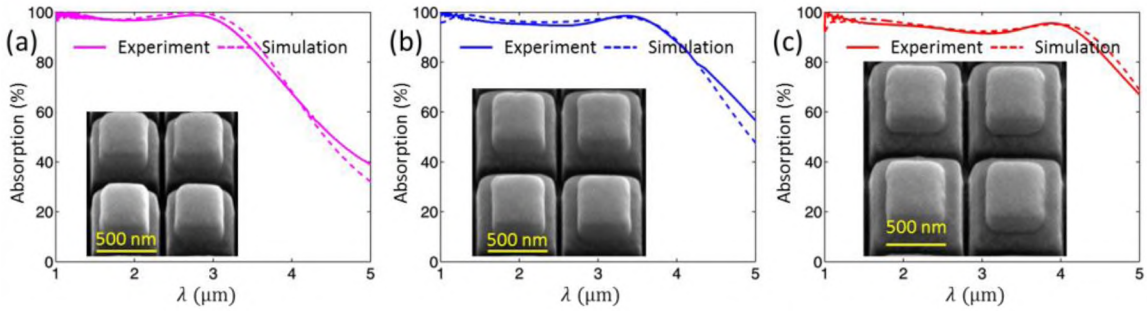

Figure 5. Experimental (solid curves) and simulated (dashed curves) absorption spectra for the double-square absorber with (a) $P = 600\text{nm}$, (b) $P = 700\text{nm}$ and (c) $P = 800\text{nm}$, respectively. The insert is the SEM image of the fabricated double-square absorber structure.

Oblique incidence is also considered to show if the designed absorber can work in different incident angles and collect more infrared light. Since the double-ring structure is symmetric, the absorption is the same for TE and TM polarizations (configurations as shown in Figures 6(a) and 6(b)) under normal incidence. However, under oblique incidence, the absorption spectra vary differently for TE and TM polarizations when considering the incident angle from $0°$ to $85°$, as shown in Figures 6(c) and 6(d) for the absorber with $P = 700\text{ nm}$. It is shown that the absorption for TM polarization can be kept around 80% even at high incident angles, while the absorption for TE polarization is

not as high as TM polarization but still remains around 70% at high incident angles. This is because the double ring resonances are magnetic resonances and the multilayer impedance match can be sustained better for TM polarization at oblique incidence. In consequence, the designed broadband infrared absorber is angle-insensitive and polarization-independent and thus it is practical for energy harvesting applications.

To further explore the two plasmonic resonances of the stacked double Cr ring resonators, optical field distributions are analyzed at the resonant wavelengths using COMSOL Multiphysics software. As shown in Figure 7(a), the two magnetic resonances can be illustrated with the normalized $|H_y|$ field profiles in $y-z$ plane. At the first magnetic resonance of $\lambda = 2.15\mu m$ dominated by the top ring, the magnetic field is mainly located between the two rings. At the second magnetic resonance of $\lambda = 3.75\mu m$ dominated by the bottom ring, the magnetic field is mostly confined between the bottom ring layer and the Cr mirror.

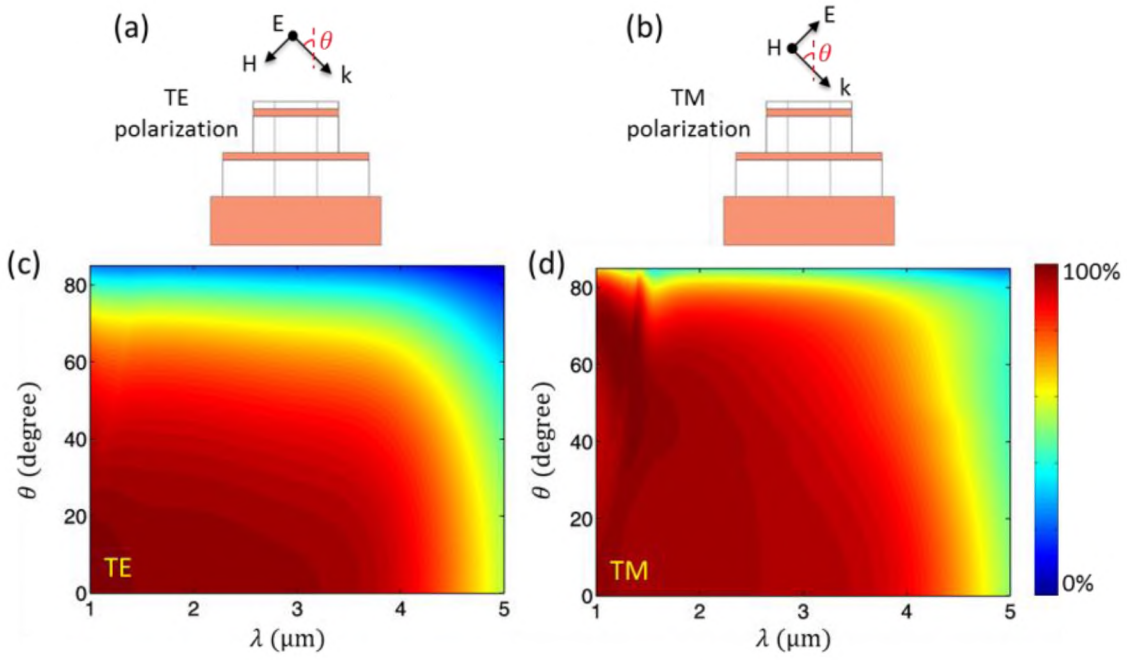

Figure 6. Absorption under oblique incidence. (a), (b) Configurations of TE polarization and TM polarization. (c), (d) Simulated absorption spectra of the double-ring absorber with $P = 700$ nm under oblique incidence for TE polarization and TM polarization, respectively.

Particularly in solar thermophotovoltaics (STPV) applications, the device working temperature is usually required to reach at least 800℃ [38–40] which approaches or even sometimes surpasses the melting points of bulk gold (1063℃) and silver (961℃) [41]. Chromium with a melting point of 1906℃ [17] utilized in infrared absorbers can stand high operating temperature. In addition, chromium is significantly cheaper than gold or silver, making chromium a reasonable choice for high-volume production of infrared absorbers. In the broadband absorber, incident light will be eventually converted into heat because of the resistive loss (R_m) of metal. In this way, the Cr ring resonators act as nanoscale heat sources resulting in the local temperature increase and eventually a thermal equilibrium will be reached since the heat is conducted away by air above the absorber structure and the Cr mirror below. To investigate the temperature distribution in the absorber, the heat transfer equation $\nabla\bullet(-k\nabla\theta)=q$ is solved, where k is the thermal conductivity and q is the heat power density generated in the Cr layers, $q(\boldsymbol{r})=(\omega/2)\,\mathrm{Im}[\varepsilon(\omega)]\varepsilon_0|\boldsymbol{E}(\boldsymbol{r})|^2$.

As shown in Figure 7(b), if a single wavelength light source (e.g. laser) with wavelength at the top ring resonance of $\lambda=2.15\mu\mathrm{m}$ is used and the incident power is $20.4\mu\mathrm{W}/\mu\mathrm{m}^2$ (corresponding to $10\mu\mathrm{W}$ light into one unit cell), the highest heat generation density is about $2.06\times10^{15}\,\mathrm{W/m^3}$ located at the top ring. If the single wavelength light source is tuned to the bottom ring resonance at $\lambda=3.75\mu\mathrm{m}$, the highest heat generation can reach $2.92\times10^{15}\,\mathrm{W/m^3}$ located at the bottom ring. At thermal equilibrium, the temperature increase distribution is a result of the balance between the heat generation and the boundary conditions where heat is conducted away. In simulation, the top and bottom boundaries are set as the fixed temperature and the side boundaries are insulated since the structure is periodic. The temperature increase distributions are plotted in Figure 7(c) at the two resonant wavelengths. According to the Fourier's law where heat transfer rate is proportional to the thermal conductivity of material and the temperature gradient as well, the highest temperature 51.3℃ is located in the top-ring for $\lambda=2.15\mu\mathrm{m}$ since heat is mostly generated in the top ring. However, for $\lambda=3.75\mu\mathrm{m}$, temperature increase in the top ring is still high (reaching to 72.7℃)

although heat is mainly generated in the bottom ring. This is because the bottom ring is close to the Cr mirror with high thermal conductivity, while dielectric layer and air has a much lower thermal conductivity.

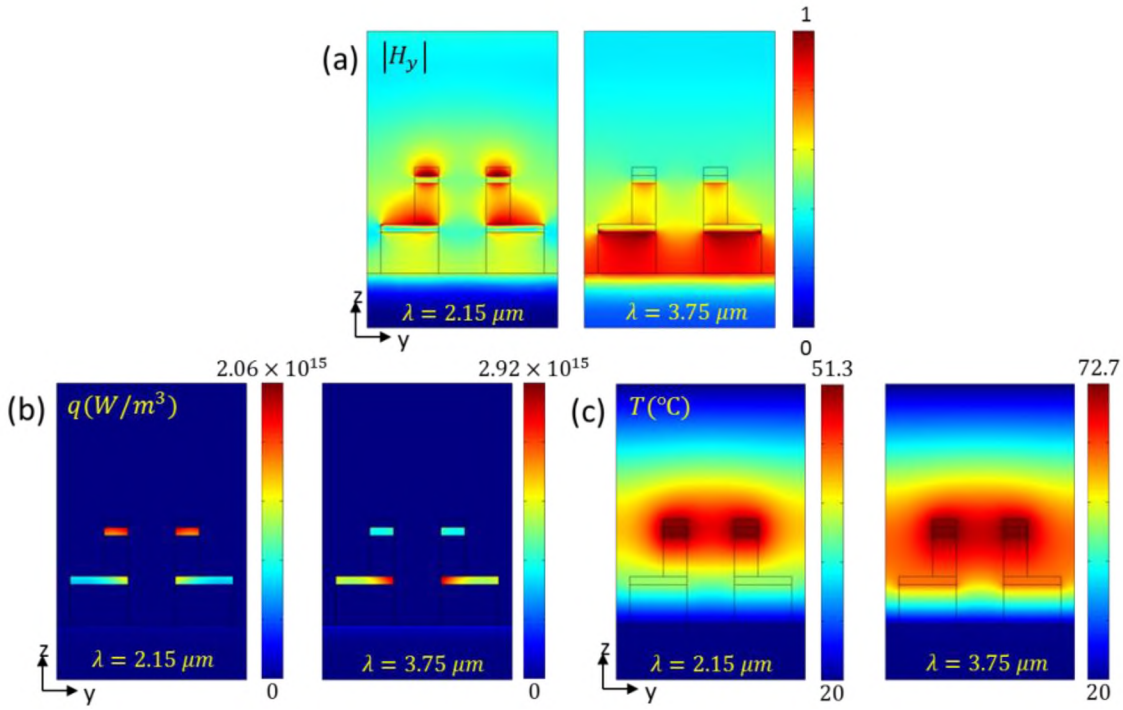

Figure 7. Resonant field profiles. (a) Normalized magnetic field distributions, (b) heat generation density distributions q and (c) temperature increase distributions T in $y-z$ plane from simulation at $\lambda = 2.15\,\mu\text{m}$ and $\lambda = 3.75\,\mu\text{m}$, respectively, for the double-ring absorber with $P = 700\,\text{nm}$ when the incident power is $20.4\,\mu\text{W}/\mu\text{m}^2$ (corresponding to $10\,\mu\text{W}$ into one unit cell).

4. CONCLUSION

A broadband infrared absorber consisting of stacked double Cr ring resonators on a Cr mirror has been designed and demonstrated with an average absorption more than 80% in 1 ~ 5 μm spectrum range. It is made of the refractory metal Cr based on the combination of two absorption mechanisms: the multilayer impedance match in the short wavelength range and the double plasmonic resonances in the long wavelength range. An equivalent circuit model has been constructed to analyze the impedance of the absorber. The designed absorber is proved to be angle-insensitive and polarization-independent under oblique incidence so that more light can be collected under different situations. The demonstrated Cr based absorber can work in high temperature environments due to the

high melting point of Cr. The demonstrated broadband Cr double-ring absorber in infrared wavelength range will advance the relevant applications such as thermophotovoltaics, solar thermophotovoltaics, thermal detection, and thermal imaging.

FUNDING

National Science Foundation (NSF) (DMR-1552871, ECCS-1653032); Office of Naval Research (ONR) (N00014-16-1-2408); U.S. Department of Energy, Office of Science, under Contract No. DE-AC02-06CH11357).

ACKNOWLEDGMENT

The authors acknowledge the facility support from the Materials Research Center at Missouri S&T. This work was performed, in part, at the Center for Nanoscale Materials, a U.S. Department of Energy Office of Science User Facility, and supported by the U.S. Department of Energy, Office of Science, under Contract No. DE-AC02-06CH11357.

REFERENCES

[1] Y. Cui, Y. He, Y. Jin, F. Ding, L. Yang, Y. Ye, S. Zhong, Y. Lin, and S. He, "Plasmonic and metamaterial structures as electromagnetic absorbers," Laser Photon. Rev. 8(4), 495–520 (2014).

[2] C. M. Watts, X. Liu, and W. J. Padilla, "Metamaterial Electromagnetic Wave Absorbers," Adv. Mater. 24(23), OP98–OP120 (2012).

[3] N. P. Sergeant, O. Pincon, M. Agrawal, and P. Peumans, "Design of wide-angle solar-selective absorbers using aperiodic metal-dielectric stacks," Opt. Express 17(25), 22800–22812 (2009).

[4] H. Wang and L. Wang, "Perfect selective metamaterial solar absorbers," Opt. Express 21(S6), A1078–A1093 (2013).

[5] S. Molesky, C. J. Dewalt, and Z. Jacob, "High temperature epsilon-near-zero and epsilon-near-pole metamaterial emitters for thermophotovoltaics," Opt. Express 21(S1), A96–A110 (2013).

[6] W. Chihhui, N. Burton III, J. Jeremy, M. Andrew, Z. Byron, S. Steve, and S. Gennady, "Metamaterial-based integrated plasmonic absorber/emitter for solar thermo-photovoltaic systems," J. Opt. 14, 024005 (2012).

[7] H. Deng, T. Wang, J. Gao and X. Yang, "Metamaterial thermal emitters based on nanowire cavities for high-efficiency thermophotovoltaics," J. Opt. 16, 035102 (2014).

[8] X. Liu, T. Tyler, T. Starr, A. F. Starr, N. M. Jokerst, and W. J. Padilla, "Taming the Blackbody with Infrared Metamaterials as Selective Thermal Emitters," Phys. Rev. Lett. 107, 045901 (2011).

[9] K. A. Arpin, M. D. Losego, A. N. Cloud, H. Ning, J. Mallek, N. P. Sergeant, L. Zhu, Z. Yu, B. Kalanyan, G. N. Parsons, G. S. Girolami, J. R. Abelson, S. Fan, and P. V. Braun, "Three-dimensional self-assembled photonic crystals with high temperature stability for thermal emission modification," Nat Commun 4, 2630 (2013).

[10] N. I. Landy, C. M. Bingham, T. Tyler, N. Jokerst, D. R. Smith, and W. J. Padilla, "Design, theory, and measurement of a polarization-insensitive absorber for terahertz imaging," Phys. Rev. B 79, 125104 (2009).

[11] J. B. Pendry, D. Schurig, and D. R. Smith, "Controlling electromagnetic fields," Science 312(5781), 1780–1782 (2006).

[12] K. Aydin, V. E. Ferry, R. M. Briggs, and H. A. Atwater, "Broadband polarization-independent resonant light absorption using ultrathin plasmonic super absorbers," Nat Commun 2, 517 (2011).

[13] W. Wang, Y. Cui, Y. He, Y. Hao, Y. Lin, X. Tian, T. Ji, and S. He, "Efficient multiband absorber based on one-dimensional periodic metal-dielectric photonic crystal with a reflective substrate," Opt. Lett. 39(2), 331–334 (2014).

[14] J. W. Dong, G. Q. Liang, Y. H. Chen, and H. Z. Wang, "Robust absorption broadband in one-dimensional metallic-dielectric quasi-periodic structure," Opt. Express 14(5), 2014–2020 (2006).

[15] B. J. Lee and Z. M. Zhang, "Design and fabrication of planar multilayer structures with coherent thermal emission characteristics," J. Appl. Phys. 100, 063529 (2006).

[16] N. Mattiucci, M. J. Bloemer, N. Akozbek, and G. D'Aguanno, "Impedance matched thin metamaterials make metals absorbing," Sci. Rep. 3, 3203 (2013).

[17] H. Deng, Z. Li, L. Stan, D. Rosenmann, and D. Czaplewski, "Broadband perfect absorber based on one ultrathin layer of refractory metal," Opt. Lett. 40(11), 2592–2595 (2015).

[18] Y. Cui, K. H. Fung, J. Xu, H. Ma, Y. Jin, S. He, and N. X. Fang, "Ultrabroadband Light Absorption by a Sawtooth Anisotropic Metamaterial Slab," Nano Lett. 12(3), 1443–1447 (2012).

[19] D. Fei, J. Yi, C. Hao, L. Mo, F. Ding, Y. Jin, B. Li, H. Cheng, L. Mo, and S. He, "Ultrabroadband strong light absorption based on thin multilayered metamaterials," Laser Photon. Rev. 8(6), 946–953 (2014).

[20] J. Zhou, A. F. Kaplan, L. Chen, and L. J. Guo, "Experiment and Theory of the Broadband Absorption by a Tapered Hyperbolic Metamaterial Array," ACS Photonics 1(7), 618–624 (2014).

[21] D. Ji, H. Song, X. Zeng, H. Hu, K. Liu, N. Zhang, and Q. Gan, "Broadband absorption engineering of hyperbolic metafilm patterns," Sci. Rep. 4, 4498 (2014).

[22] Y. Sun, B. Edwards, A. Alù, and N. Engheta, "Experimental realization of optical lumped nanocircuits at infrared wavelengths," Nat Mater 11(3), 208–212 (2012).

[23] D. Zhu, M. Bosman, and J. K. W. Yang, "A circuit model for plasmonic resonators," Opt. Express 22(8), 9809-9819 (2014).

[24] M. Staffaroni, J. Conway, S. Vedantam, J. Tang, and E. Yablonovitch, "Circuit analysis in metal-optics," Phot. Nano. Fund. Appl. 10(1), 166–176 (2012).

[25] Q. Zhang, L. Bai, Z. Bai, P. Hu, and C. Liu, "Theoretical analysis and design of a near-infrared broadband absorber based on EC model," Opt. Express 23(7), 8910–8917 (2015).

[26] E. D. Palik, Handbook of Optical Constants of Solids (Academic, New York, 1985).

[27] D. Barchiesi and T. Grosges, "Fitting the optical constants of gold, silver, chromium, titanium, and aluminum in the visible bandwidth," J. Nanophoton. 8(1), 083097 (2014).

[28] A. D. Rakic, A. B. Djurišić, J. M. Elazar, and M. L. Majewski, "Optical properties of metallic films for vertical-cavity optoelectronic devices," Appl. Opt. 37, 5271-5283 (1998).

[29] N. Moshonas, G. K. Pagiatakis, and N. A. Stathopoulos, "Application of the transmission line method for the study of highly nonlinear multilayer optical structures," Opt. Eng. 53(11), 115106 (2015).

[30] H. A. Haus, Waves and fields in optoelectronics (Prentice-Hall, Inc., Englewood Cliffs, N.J., 1984).

[31] D. Cheng, J. Xie, P. Zhou, H. Zhang, N. Zhang, and L. Deng, "Numerical study of a new negative index material in mid-infrared spectrum," Opt. Express 20(23), 25744–25751 (2012).

[32] J. Zhou, E. N. Economon, T. Koschny, and C. M. Soukoulis, "Unifying approach to left-handed material design," Opt. Lett. 31(24), 3620–3622 (2006).

[33] S. Ghosh and K. V Srivastava, "An Equivalent Circuit Model of FSS-Based Metamaterial Absorber Using Coupled Line Theory," Antennas Wirel. Propag. Lett. IEEE 14, 511–514 (2015).

[34] Y. Pang, H. Cheng, Y. Zhou, and J. Wang, "Analysis and design of wired-based metamaterial absorbers using equivalent circuit approach," J. Appl. Phys. 113, 114902 (2013).

[35] J. Zhou, L. Zhang, G. Tuttle, T. Koschny, and C. M. Soukoulis, "Negative index materials using simple short wire pairs," Phys. Rev. B 73, 041101(R) (2006).

[36] S. Bhattacharyya, S. Ghosh, and K. V. Srivastava, "Equivalent circuit model of an ultra-thin polarization-independent triple band metamaterial absorber," AIP Adv. 4, 097127 (2014).

[37] J. G. Hong and M. J. Lancaster, Microstrip Filters for RF/Microwave Applications (John Wiley & Sons, Inc., New York, 2001).

[38] W. Li, U. Guler, N. Kinsey, G. V Naik, A. Boltasseva, J. Guan, V. M. Shalaev, and A. V Kildishev, "Refractory Plasmonics with Titanium Nitride: Broadband Metamaterial Absorber," Adv. Mater. 26(47), 7959–7965 (2014).

[39] P. Nagpal, S. E. Han, A. Stein, and D. J. Norris, "Efficient low-temperature thermophotovoltaic emitters from metallic photonic crystals," Nano Lett. 8(10), 3238–3243 (2008).

[40] A. Narayanaswamy and G. Chen, "Surface modes for near field thermophotovoltaics," Appl. Phys. Lett. 82, 3544–3546 (2003).

[41] E. Rephaeli and S. Fan, "Absorber and emitter for solar thermo-photovoltaic systems to achieve efficiency exceeding the Shockley-Queisser limit," Opt. Express 17(17), 15145–15159 (2009).

IV. ULTRA-BROADBAND ABSORPTION IN INFRARED BY TAPERED HYPERBOLIC WAVEGUIDE ABSORBER MADE OF 13-PAIR AU-SIO2 MULTILAYER

Huixu Deng, Liliana Stan, David A. Czaplewski, Jie Gao, and Xiaodong Yang

Department of Mechanical and Aerospace Engineering

Missouri University of Science and Technology, Rolla, Missouri 65409, U.S.A.

ABSTRACT

The ultra-broadband absorption covering a range of $\lambda = 1{\sim}6$ μm with average amplitude of 95% is realized by the designed tapered hyperbolic waveguide absorber which is made of 13-pair Au-SiO_2 multilayer on glass. The absorption is broadband since stop light with different wavelengths can be obtained at different waveguide widths in the tapered waveguide. A planar hyperbolic waveguide model is built to determine the stop light by considering the forward and backward guided modes. In simulation, the stop light fields located at each metal layer are plotted out and the stop light modes can be found at the absorption peaks calculated by reducing the Au loss manually. In experiment, six waveguide absorber samples with different top width were fabricated and the absorption ranges were measured. The relation between the waveguide width and the stop light wavelength turns out to be almost linear from all the results in theory, simulation and experiment. To show the designed absorber is practical in the applications of energy harvesting, the waveguide absorber is demonstrated to be angle-insensitive and polarization-independent, and the heat generation and temperature increase are also discussed.

Keywords: Absorption, Energy transfer, Metamaterials, Infrared

1. INTRODUCTION

Broadband absorbers in infrared (IR) range have been one of the most exciting issues in these few years [1], [2] since they are crucial in various applications, such as solar energy harvesting [3], [4], thermophotovoltaic energy conversion [5], thermal emission [6] and thermal imaging [7]. There are diverse methods to obtain broadband

absorption based on different mechanisms including combining multiple resonances on the same metasurface [4], [8], exciting phase resonances in planar metal-dielectric stacks [9], [10], achieving impedance match for multilayers [11], [12]. In addition, it is also possible to get broadband (even ultra-broadband) absorption by generating stop light modes in the tapered hyperbolic waveguides [13]–[17]. Cui *et al.* [13] demonstrated the ultra-broadband absorption to be higher than 95% in $\lambda = 3 \sim 5.5\mu m$ in theory and simulation. Ding *et al.* [14] achieved broadband absorption over 90% in $\lambda = 0.4 \sim 3.6\mu m$ utilizing the high loss metal of Chromium (Cr) in experiment. Zhou *et al.* [17] also fabricated a 9-stack Au-Al_2O_3 tapered structure resulting in absorption in $\lambda = 1.5 \sim 3\mu m$ and an 11-stack Au-Ge tapered structure resulting in absorption in $\lambda = 2.5 \sim 6\mu m$. All the works proved that stop light in tapered hyperbolic waveguide is a robust way to get ultra-broadband absorption. However, the works were not able to fully utilize the stop light effect and to experimentally realize the absorption with ultra-broadband and high amplitude at the same time by using metal with relatively low loss. In this paper, the ultra-broadband absorption covering a range of $\lambda = 1 \sim 6\mu m$ with average amplitude of 95% is realized by the designed tapered hyperbolic waveguide absorber which is made of 13-pair Au-SiO_2 multilayer on glass. The absorption can be ultra-broadband since stop light with different wavelengths can be achieved at different waveguide widths in the tapered waveguide. The relation between the waveguide width and the stop light wavelength is proved to be almost linear from all the results in theory, simulation and experiment.

2. DESIGN AND THEORY

The schematic of the proposed tapered waveguide absorber is comprised of 13-pair Au and SiO_2 layers on glass (which is SiO_2 as well) as shown in Figure 1(a). The Au layer thickness is $t_m = 20\text{nm}$ and the SiO_2 layer thickness is $t_d = 80\text{nm}$. In one unit cell with period of $P = 1500\text{nm}$, the top width of the tapered waveguide is $W_t = 250\text{nm}$ and the bottom width is the same as the period. As shown in Figure 1(b), while the permittivity of SiO_2 is a constant $\varepsilon_d = 2.1$, the permittivity of Au can be calculated using Drude model $\varepsilon_m = 1 - \omega_p^2 / \omega(\omega + i\gamma)$ where ω is the frequency, $\omega_p = 1.37 \times 10^{16}\, rad/s$ is

the plasma frequency and $\gamma = 3\gamma_0 = 12.24 \times 10^{13}\ rad/s$ is the bulk collision frequency (the material loss) and three times of the original value.

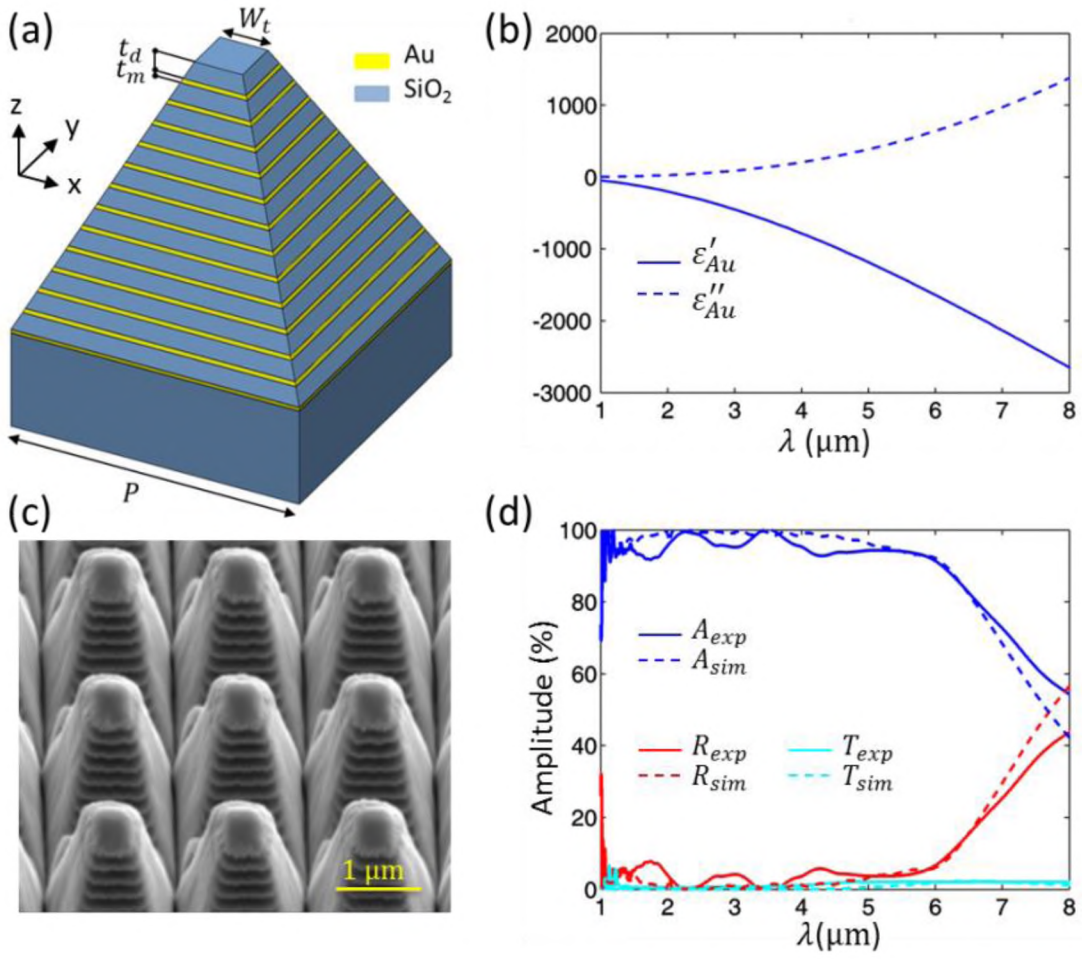

Figure 1. Design of the tapered waveguide absorber. (a) Schematic of the tapered waveguide absorber consisting of 13 pairs of Au-SiO_2 layers. (b) Permittivity of Au based on the Drude model when the loss is $\gamma = 3\gamma_0$. (c) SEM image of the fabricated waveguide absorber with $P = 1500\text{nm}$ and $W_t = 250\text{nm}$. (d) Spectra of absorption A (in blue), reflection R (in red) and transmission T (in cyan) from experiment (solid curves) and simulation (dashed curves), respectively.

A sample of the tapered waveguide absorber was fabricated using Focused Ion Beam (FIB) and the tapered structure was achieved by controlling the dwell time of the ion beam milling at different milling depth. From its SEM image as shown in Figure 1(c), it is clear to see the Au-SiO_2 layer pairs in the tapered waveguide and some fabrication

defects like coatings on the both sides of the taper are due to the Ga pollution during the long time ion beam milling. Different from most other absorber designs in which a thick metal mirror is used as substrate to eliminate transmission, the proposed absorber stands on glass and transmission is allowed. Thus, the spectra of transmission T (in cyan) and reflection R (in red) were measured using Fourier transform infrared spectroscopy (FTIR), and the absorption can be calculated as $A=1-T-R$ (in blue) as shown in Figure 1(d), respectively. Since the transmission is close to zero due to the stop light phenomenon, the absorption can reach 95% in average covering the range of $\lambda=1\sim6\mu\text{m}$. The simulation results (dashed curves) calculated by COMSOL are also shown in Figure 1(d) and in good agreement with the experiment results (solid curves).

To explain why the broadband absorption can be achieved in the tapered waveguide absorber, a cladding/core/cladding planar waveguide model is built up. Due to the symmetry in x and y directions, the Au-SiO_2 multilayer tapered waveguide can be regarded as a tapered waveguide with different width along the z direction and infinite long in y direction. As the light propagates in the waveguide along z direction, the change of waveguide width will lead to the change of waveguide mode. Thus, the whole tapered waveguide can be treated as a combination of infinite slices of waveguide with different widths stacked in the z direction, and each slice of waveguide with a waveguide width W is illustrated in Figure 2(a). The core represents the hyperbolic waveguide with tensor permittivity of $\vec{\varepsilon}=\vec{\varepsilon}_x+\vec{\varepsilon}_y+\vec{\varepsilon}_z$, and the claddings on the two sides are air with permittivity of $\varepsilon_1=1$. The core permittivity can be evaluated via the effective media theory for the Au-SiO_2 multilayer as $\vec{\varepsilon}_x=f_m\varepsilon_m+(1-f_m)\varepsilon_d$, $\vec{\varepsilon}_z=1/\left(f_m/\varepsilon_m+(1-f_m)/\varepsilon_d\right)$ in which f_m is the filling ratio of metal. Since the Au-SiO_2 multilayer is symmetric in x and y directions, $\vec{\varepsilon}_x$ is equal to $\vec{\varepsilon}_y$. It can be seen from Figure 2(b) that the waveguide is hyperbolic since $\vec{\varepsilon}_x$ is negative and $\vec{\varepsilon}_z$ is positive.

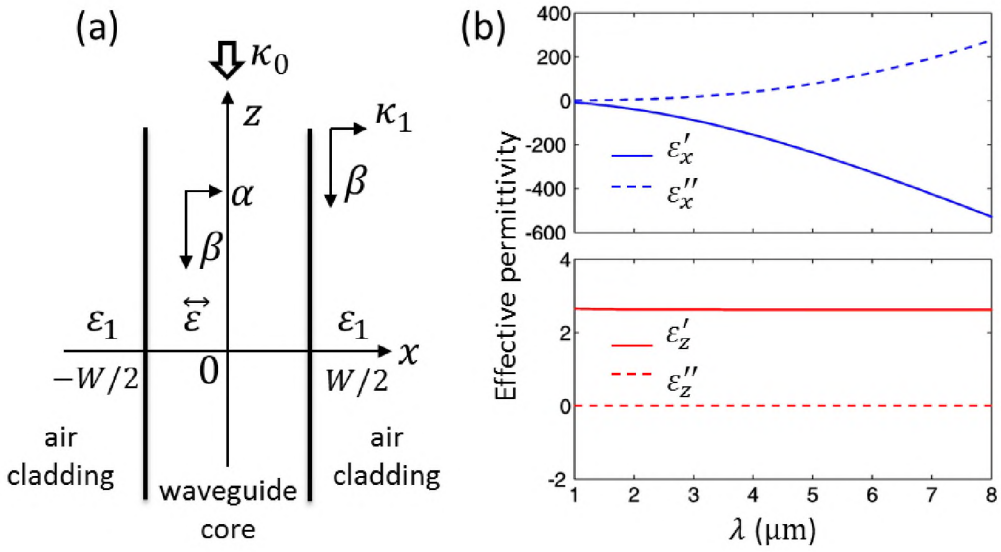

Figure 2. Waveguide model in 2-D. (a) Schematic of the 2-D waveguide model where the core represents the hyperbolic waveguide based on the effective media of Au-SiO_2 multilayer and the claddings represent the air. (b) Effective permittivity of the Au-SiO_2 multilayer in x direction ε_x (in blue and equal to ε_y in y-direction) and in z direction ε_z (in red).

To illustrate how the stop light is obtained, the forward and backward guided modes inside the waveguide are solved by considering the continuous boundary condition at $x = \pm W/2$ (Eq. 1) and the dispersion relation (Eq. 2) [18]:

$$\kappa_1 W = \pm \frac{\varepsilon_1}{\varepsilon_z} \alpha W \left(\tan \frac{\alpha W}{2} \right)^{\pm 1} \tag{1}$$

$$\left(\kappa_1 W\right)^2 + \frac{\varepsilon_x}{\varepsilon_z}\left(\alpha W\right)^2 = \kappa_0^2 W^2 \left(\varepsilon_x - \varepsilon_1\right) \tag{2}$$

where $\kappa_0 = 2\pi/\lambda$ is the wave vector of the incident light in vacuum, $\kappa_1^2 = \beta^2 - \kappa_0^2 \varepsilon_1$ and $\alpha = \sqrt{\left|\frac{\varepsilon_z}{\varepsilon_x}\left(\beta^2 - \kappa_0^2 \varepsilon_x\right)\right|}$. β is the wave vector in z direction and should be equal in both the waveguide core and the air claddings. However, the wave vector in x direction would be different: in the air claddings, the wave vector in x is κ_1, while in the waveguide core, the wave vector is α. After solving these two equations, the wave vectors can be got and

thus the effective index of the waveguide can be calculated by $n_{eff} = n_{eff}^{'} + in_{eff}^{''} = \beta / \kappa_0$. Since there are two roots found during solving the equations, it indicates that the hyperbolic waveguide can support two waveguide guided modes at the same time: the forward guided mode where the phase velocity direction is the same as the group velocity direction and the backward guided mode where these two velocity directions are opposite. As shown in Figures 3(a) and (b), the real and imaginary parts of the effective index are plotted out as a function of the waveguide width W for different incident wavelengths $\lambda = 1, 3 \text{and} 5 \mu\text{m}$. The blue curves indicate that the effective indices of forward guided modes get higher as the waveguide width becomes larger. On the other hand, the effective indices of backward guided modes get decreased as the waveguide width becomes larger. As a result, the effective indices of both the forward and backward modes will finally merge at a proper waveguide width. In this way, the stop light is achieved since its group velocity can approach to zero and light will be absorbed at this place. For instance, when the incident wavelength is $\lambda = 5 \mu\text{m}$, the stop light is located around $W \approx 1340 \text{nm}$ as the green region shown in Figures 3(a) and (b). The relation between the stop light wavelength and the waveguide width turns out to be almost linear as the magenta line shown in Figure 3(c). As the incident wavelength increases, the waveguide width where the stop light is located will also increase.

In order to show the stop light in the hyperbolic waveguide in details, the loss of Au is reduced manually to $\gamma = \gamma_0$ and the absorption is recalculated in COMSOL for the tapered waveguide absorber with $P = 1500 \text{nm}$ and $W_t = 250 \text{nm}$. The spectra of transmission (in cyan), reflection (in red) and absorption (in blue) for both $\gamma = 3\gamma_0$ and $\gamma = \gamma_0$ are shown in Figure 4(a), respectively. It is obvious to see the absorption peaks for Au loss of $\gamma = \gamma_0$ representing the stop light occurs at each Au metal layer with different waveguide width. Specifically, for the absorption peak at the wavelength of $\lambda = 6.0 \mu\text{m}$, the stop light can be observed at the second bottom metal layer in the tapered waveguide as the magnetic field $|H|$ shown in Figure 4(b). As the metal layer width becomes smaller from bottom to top, the wavelength of each stop light gets shorter. Consequently, the absorption of the whole tapered waveguide is broadband covering the range of

$\lambda = 1 \sim 6\mu m$ with average amplitude of 95%. However, for the stop light at the first bottom metal layer when the wavelength is $\lambda = 6.52\mu m$, its corresponding absorption peak is hidden in the decline part of the absorption spectrum. This is because the guided modes are weak at the very bottom since the first bottom metal layer is like the end of the hyperbolic waveguide and there is no mirror substrate in below.

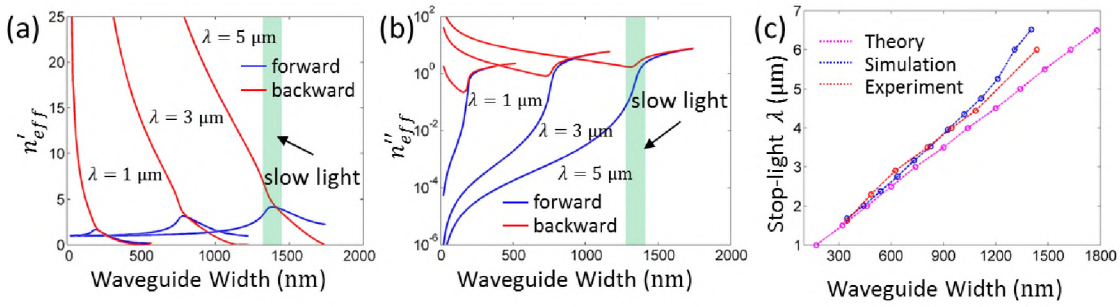

Figure 3. Stop light predicted by the waveguide model. (a) and (b) are the effective index ($n_{eff} = n'_{eff} + in''_{eff}$) of the guided forward (in blue) and backward (in red) modes at $\lambda = 1, 3, \text{and} 5\mu m$, respectively. The green region is the stop light mode at $\lambda = 5\mu m$ where the forward and backward modes merge at the same waveguide width. (c) Relation between the stop light wavelength and its corresponding waveguide width from theory (in magenta), simulation (in blue) and experiment (in red), respectively.

It is also hard to determine the absorption peak with $\lambda = 1.68\mu m$ for the stop light at the first top metal layer in the spectra since there are too many sharp peaks in the range of $\lambda = 1 \sim 2\mu m$. They are caused by the high order modes at the waveguide bottom where the waveguide width is large. The relation between the stop light wavelength and the waveguide width can be also evaluated from the simulation result as the blue curve in Figure 3(c). Each blue dot represents the absorption peak wavelength and its corresponding waveguide width (the metal layer width) where the stop light is located. It can be seen that the simulation results are very close to the theoretical predictions (blue line in Figure 3(c)) when the waveguide width is much smaller than the structure period $P = 1500\text{nm}$, but get away from that when the waveguide width approaches to $P = 1500\text{nm}$. This is because when the waveguide width is close to the period, there exists the Bloch mode due to the overlap of the evanescent fields between every two neighboring tapered waveguides [14], [16].

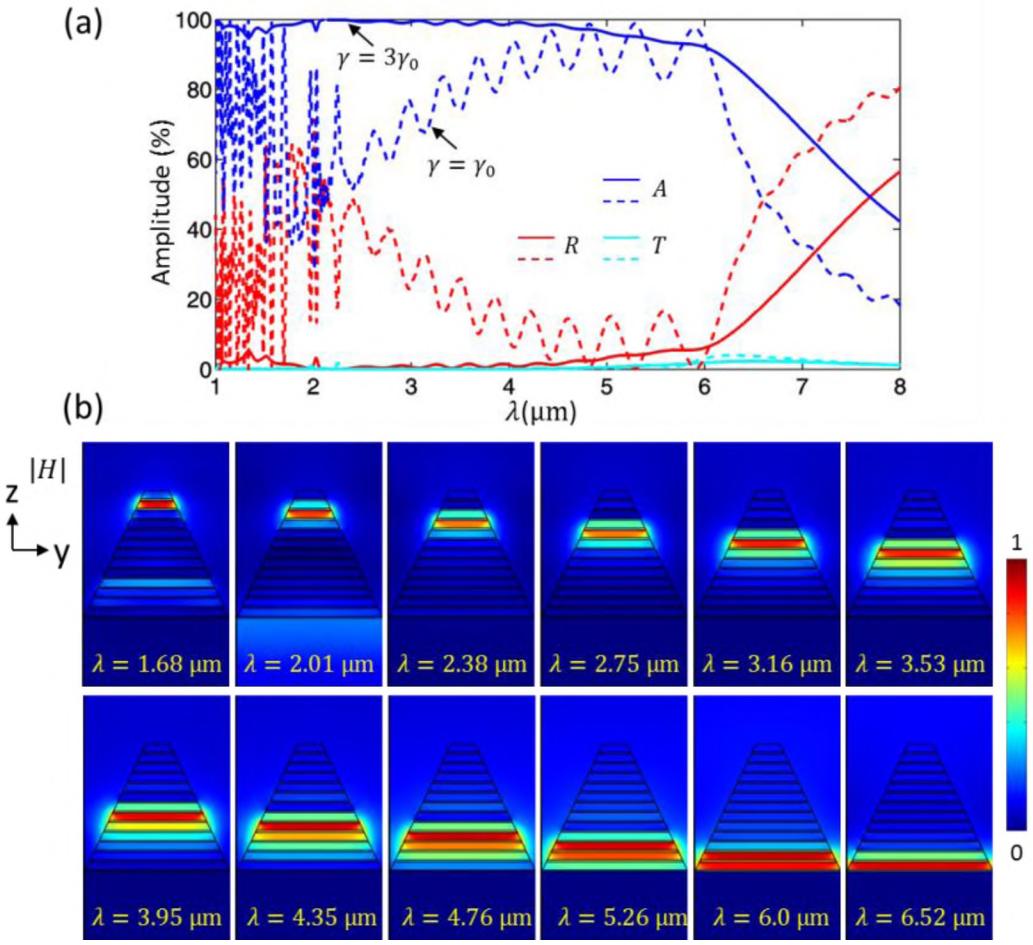

Figure 4. Stop light in simulation. (a) Spectra of absorption A (in blue), reflection R (in red) and transmission T (in cyan) for the tapered waveguide absorber with $\mathrm{P}=1500\,\mathrm{nm}$, $W_t = 250\mathrm{nm}$ and Au loss of $\gamma = 3\gamma_0$ (solid curves) and $\gamma = \gamma_0$ (dashed curves), respectively. (b) Magnetic fields $|H|$ in the y-z plane for the tapered waveguide absorber in (a) with $\gamma = 3\gamma_0$ at each peak wavelength, respectively.

3. RESULTS AND DISCUSSION

The relation between the absorption range and the waveguide width is also proved in experiment by changing the waveguide top width. As shown in Figures 5 (a)-(f), six samples were fabricated with $P = 1500\mathrm{nm}$ and $W_t = 250, 400, 550, 750, 900$ and $1050\mathrm{nm}$, respectively. The scalar bar in each figure is $1\mu\mathrm{m}$. The spectra of absorption A (in blue), reflection R (in red) and transmission T (in cyan) for each fabricated sample were also measured as shown in Figures 6(a)-(f), respectively. The spectra from simulation (dashed curves) are able to match the experiment results (solid curves) very well. And as the top

width is decreased, the absorption range shrinks due to the right shift of the absorption peak determined by the top layer. The absorption peak determined by the bottom layer remains at the same wavelength since the period and waveguide bottom width of all the samples are almost unchanged.

The relation between the waveguide width and the absorption range (or the stop light wavelength) is summarized as the red curve shown in Figure 3(c). Each red dot on the red curve represents the stop light at the top metal layer of each sample except for the last red dot which represents the stop light at the bottom metal layer shared by every sample. For example, for the sample with $W_t = 1050\,\text{nm}$, its top metal layer width is $W = 1085\,\text{nm}$ leading to a stop light wavelength of $\lambda = 4.4\,\mu\text{m}$. And the width of the second bottom metal layer is $W = 1465\,\text{nm}$ resulting in a stop light at $\lambda = 6.0\,\mu\text{m}$. Thus, the absorption range of this sample is $\lambda = 4.29 \sim 6.0\,\mu\text{m}$. The absorption ranges of all the other samples are measured in the same way with respect to the top metal layer width, and all the red dots can be connected to an almost linear curve close to the simulation results (blue curve in Figure 3(c)) and the theoretical predictions (magenta curve in Figure 3(c)). As mentioned above, as the waveguide width approaches to the structure period, the stop light wavelength will get away from the theoretical predictions due to the Bloch mode.

In order to collect more light, the absorption under oblique incidence is considered. As shown in Figure 7(a), when the light is incident with an angle θ under TE polarization, the magnetic field H is tilted and the electric field E is always unchanged and perpendicular to the cross-section plane. The TM polarization case is vice versa as shown in Figure 7(b). Since the waveguide propagation modes are mainly dominated by the electric field (seen from Eqs. 1 and 2), the absorption for TE polarization can be kept in the wavelength range of $\lambda = 1 \sim 7\,\mu\text{m}$ with absorption more than 80% even at high incident angles, while the absorption for TM polarization is not as good as TE but still remains in the range of $\lambda = 1 \sim 6\,\mu\text{m}$ at high incident angles. In consequence, the designed tapered waveguide absorber is angle-insensitive and polarization-independent and thus practical in the applications of energy harvesting.

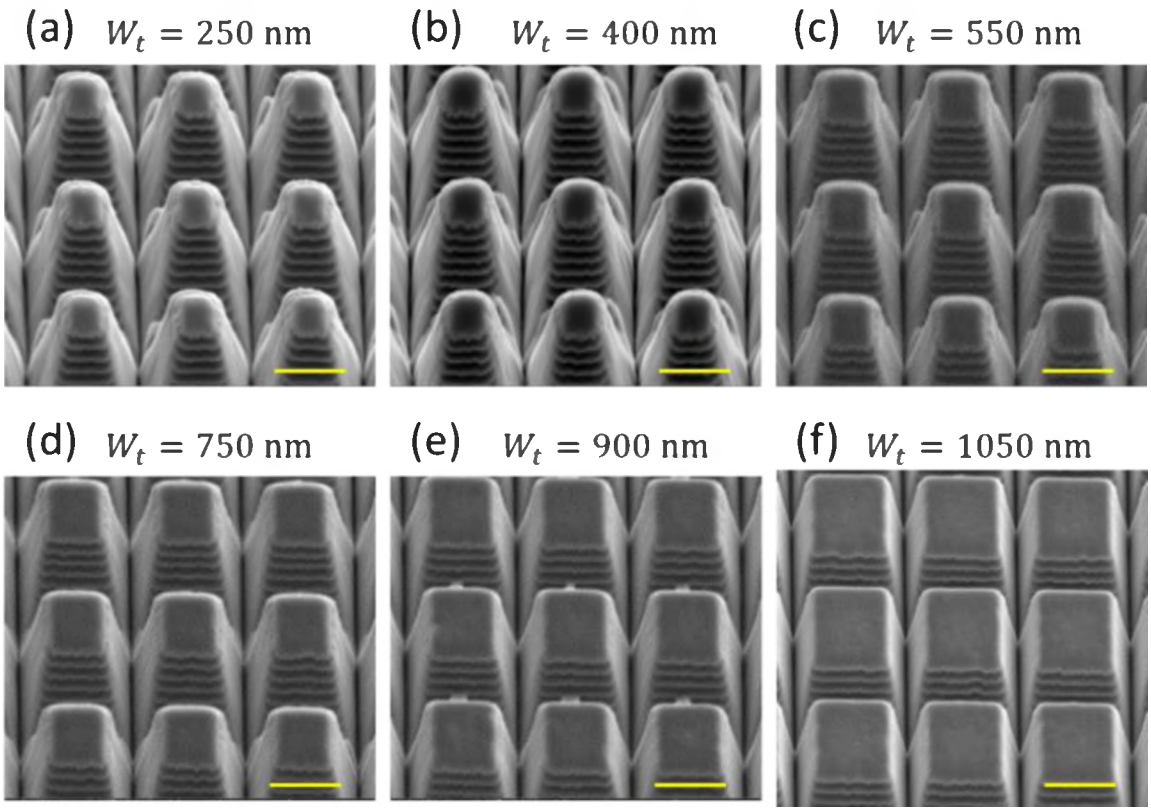

Figure 5. Experiment fabrication of the waveguide absorber. (a)-(f) are the SEM images of the fabricated tapered waveguide absorbers with $P = 1500\text{nm}$ and $W_t = 250, 400, 550, 750, 900$ and 1050nm, respectively. The scale bar in each figure is $1\mu\text{m}$.

To investigate the temperature distribution T in the absorber, the heat transfer equation $\nabla \bullet (-k\nabla T) = q$ is solved, where k is the thermal conductivity and q is the heat generation density in the lossy metal, $q(\boldsymbol{r}) = (\omega/2)\,\text{Im}\left[\varepsilon(\omega)\right]\varepsilon_0 \left|\boldsymbol{E}(\boldsymbol{r})\right|^2$. As shown in Figure 8, the heat generation density is located where the $|E|$ field is concentrated in the metal since q is proportional to $\sim \text{Im}\left[\varepsilon(\omega)\right]\left|\boldsymbol{E}(\boldsymbol{r})\right|^2$. Particularly, with an incident light power of $10\mu\text{W}$ onto one unit cell (corresponding to $4.44\mu\text{W}/\mu\text{m}^2$), the heat generation density can be $2.64\times10^{13} \sim 2.94\times10^{14}\,\text{W}/\text{m}^3$ at different metal layers where the stop light is obtained under different wavelengths.

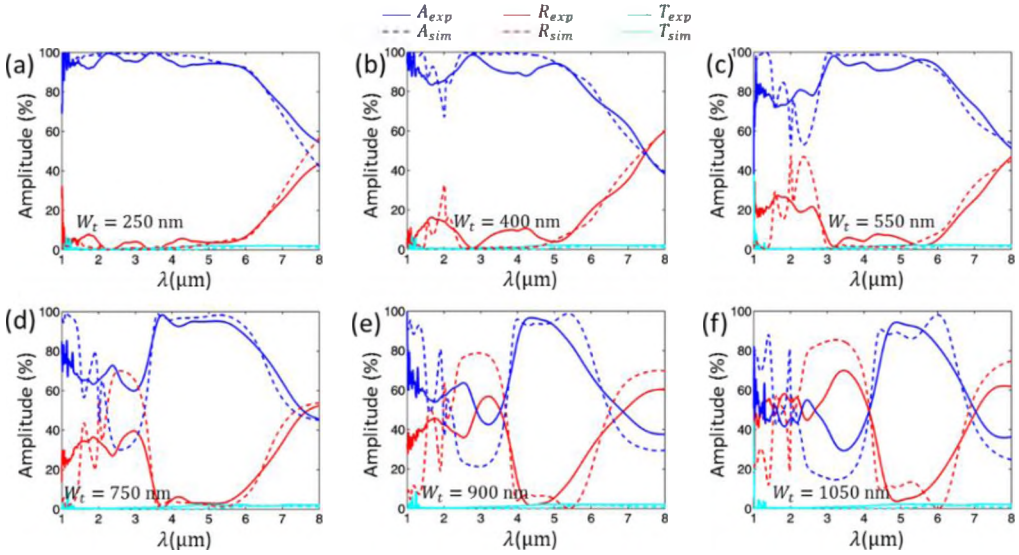

Figure 6. Experiment measurement of the waveguide absorber. (a)-(f) are the spectra of absorption A (in blue), reflection R (in red) and transmission T (in cyan) for the tapered waveguide absorbers with $P = 1500\text{nm}$ and $W_t = 250, 400, 550, 750, 900$ and 1050nm, respectively.

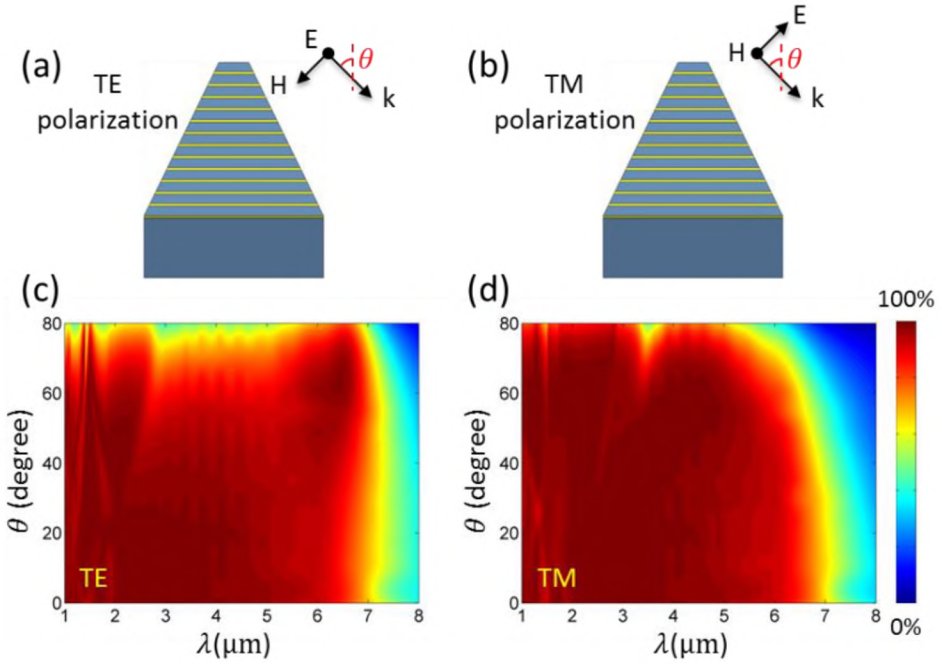

Figure 7. Absorption under oblique incidence. (a), (b) Configurations of TE polarization and TM polarization, respectively. (c), (d) Simulated absorption of the tapered waveguide absorber under oblique incidence for TE polarization and TM polarization, respectively.

Correspondingly, the highest temperature is always found at the place where the heat is generated. As shown in Figure 9, the temperature distributions at different stop light wavelengths are plotted. When the wavelength is short and the stop light is obtained at the top of the tapered waveguide, the highest temperature is also at the top and gets lower quickly to the bottom.

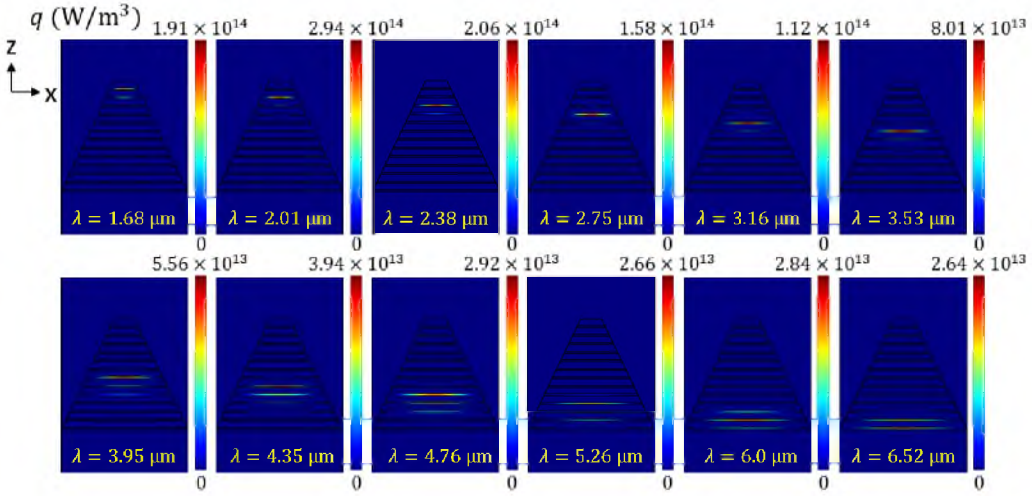

Figure 8. Heat generation fields q in the x-z plane for the tapered waveguide absorber with $P = 1500\,\text{nm}$, $W_t = 250\,\text{nm}$ and $\gamma = 3\gamma_0$ at each stop light wavelength, respectively.

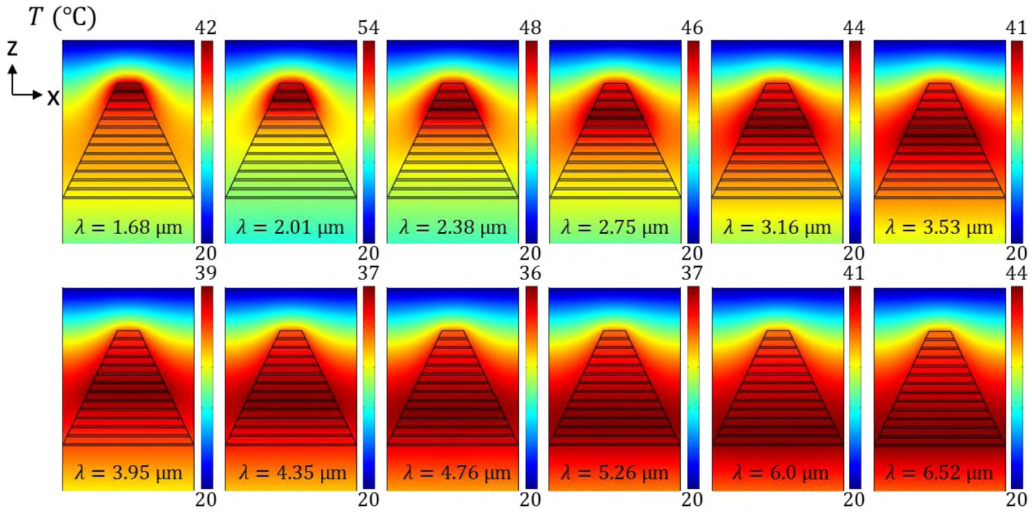

Figure 9. Temperature fields T in the x-z plane for the tapered waveguide absorber with $P = 1500\,\text{nm}$, $W_t = 250\,\text{nm}$ and $\gamma = 3\gamma_0$ at each stop light wavelength, respectively.

However, when the wavelength is long and the highest temperature is located at the waveguide bottom, the whole waveguide is warmed up and the temperature gradient along z direction is small. This is because air has a much lower conductivity compared with the glass substrate, and to conduct the same amount of heat away, it needs a larger temperature gradient.

4. CONCLUSIONS

In conclusion, a tapered waveguide absorber made of 13-pair Au-SiO_2 multilayer is designed and the ultra-broadband absorption due to stop light phenomenon is realized experimentally. For the fabricated absorber sample with $P = 1500\text{nm}$ and $W_t = 250\text{nm}$, the absorption can reach 95% in average covering the range of $\lambda = 1 \sim 6\mu\text{m}$. A cladding/core/cladding planar waveguide model is used to explore the relation between the stop light wavelength and the waveguide width. The stop light can be achieved at a proper waveguide width where the forward and backward guide modes have the same effective index. And it turns out that the stop light wavelength increases linearly with the waveguide width. This linear relation can be also observed in the simulation results by reducing the Au loss manually and plotting out the magnetic field at each absorption peak wavelength. In experiment, the linear relation can be proved one more time by measuring the absorption range of the six fabricated waveguide absorber samples with different top width. The absorption range shrinks as the top width gets larger due to the red shift of the stop light wavelength at the top metal layer. The tapered waveguide absorber is proved to be angle-insensitive and polarization-independent by considering the absorption under angled incidence for TE/TM polarizations. And the heat generation fields and temperature fields are also discussed to show the designed absorber is practical in the applications of energy harvesting.

FUNDING

National Science Foundation (NSF) (DMR-1552871, ECCS-1653032); Office of Naval Research (ONR) (N00014-16-1-2408); U.S. Department of Energy, Office of Science, under Contract No. DE-AC02-06CH11357).

ACKNOWLEDGMENT

The authors acknowledge the facility support from the Materials Research Center at Missouri S&T. This work was performed, in part, at the Center for Nanoscale Materials, a U.S. Department of Energy Office of Science User Facility, and supported by the U.S. Department of Energy, Office of Science, under Contract No. DE-AC02-06CH11357.

REFERENCES

[1] Y. Cui, Y. He, Y. Jin, F. Ding, L. Yang, Y. Ye, S. Zhong, Y. Lin, and S. He, "Plasmonic and metamaterial structures as electromagnetic absorbers," Laser Photon. Rev. 8(4), 495–520 (2014).

[2] C. M. Watts, X. Liu, and W. J. Padilla, "Metamaterial Electromagnetic Wave Absorbers," Adv. Mater. 24(23), OP98–OP120 (2012).

[3] N. P. Sergeant, O. Pincon, M. Agrawal, and P. Peumans, "Design of wide-angle solar-selective absorbers using aperiodic metal-dielectric stacks," Opt. Express 17(25), 22800–22812 (2009).

[4] H. Wang and L. Wang, "Perfect selective metamaterial solar absorbers," Opt. Express 21(S6), A1078–A1093 (2013).

[5] H. Deng, T. Wang, J. Gao and X. Yang, "Metamaterial thermal emitters based on nanowire cavities for high-efficiency thermophotovoltaics," J. Opt. 16, 035102 (2014).

[6] X. Liu, T. Tyler, T. Starr, A. F. Starr, N. M. Jokerst, and W. J. Padilla, "Taming the Blackbody with Infrared Metamaterials as Selective Thermal Emitters," Phys. Rev. Lett. 107, 045901 (2011).

[7] N. I. Landy, C. M. Bingham, T. Tyler, N. Jokerst, D. R. Smith, and W. J. Padilla, "Design, theory, and measurement of a polarization-insensitive absorber for terahertz imaging," Phys. Rev. B 79, 125104 (2009).

[8] K. Aydin, V. E. Ferry, R. M. Briggs, and H. A. Atwater, "Broadband polarization-independent resonant light absorption using ultrathin plasmonic super absorbers," Nat Commun 2, 517 (2011).

[9] W. Wang, Y. Cui, Y. He, Y. Hao, Y. Lin, X. Tian, T. Ji, and S. He, "Efficient multiband absorber based on one-dimensional periodic metal-dielectric photonic crystal with a reflective substrate," Opt. Lett. 39(2), 331–334 (2014).

[10] J. W. Dong, G. Q. Liang, Y. H. Chen, and H. Z. Wang, "Robust absorption broadband in one-dimensional metallic-dielectric quasi-periodic structure," Opt. Express 14(5), 2014–2020 (2006).

[11] N. Mattiucci, M. J. Bloemer, N. Akozbek, and G. D'Aguanno, "Impedance matched thin metamaterials make metals absorbing," Sci. Rep. 3, 3203 (2013).

[12] H. Deng, Z. Li, L. Stan, D. Rosenmann, and D. Czaplewski, "Broadband perfect absorber based on one ultrathin layer of refractory metal," Opt. Lett. 40(11), 2592–2595 (2015).

[13] Y. Cui, K. H. Fung, J. Xu, H. Ma, Y. Jin, S. He, and N. X. Fang, "Ultrabroadband Light Absorption by a Sawtooth Anisotropic Metamaterial Slab," Nano Lett. 12(3), 1443–1447 (2012).

[14] D. Fei, J. Yi, C. Hao, L. Mo, F. Ding, Y. Jin, B. Li, H. Cheng, L. Mo, and S. He, "Ultrabroadband strong light absorption based on thin multilayered metamaterials," Laser Photon. Rev. 8(6), 946–953 (2014).

[15] D. Ji, H. Song, X. Zeng, H. Hu, K. Liu, N. Zhang, and Q. Gan, "Broadband absorption engineering of hyperbolic metafilm patterns," Sci. Rep. 4, 4498 (2014).

[16] H. Hu, D. Ji, X. Zeng, K. Liu, and Q. Gan, "Rainbow Trapping in Hyperbolic Metamaterial Waveguide," Sci. Rep. 3, 1249 (201.

[17] J. Zhou, A. F. Kaplan, L. Chen, and L. J. Guo, "Experiment and Theory of the Broadband Absorption by a Tapered Hyperbolic Metamaterial Array," ACS Photonics 1(7), 618–624 (2014).

[18] G. Xu, T. Pan, T. Zang, and J. Sun, "Characteristics of guided waves in indefinite-medium waveguides," Opt. Commun. 281(10), 2819–2825 (2008).

SECTION

2. CONCLUSION

In conclusion, various metamaterial absorbers are explored and discussed in this project. Different mechanisms are analyzed in detail leading to the design and optimization of different absorbers to achieve narrowband or broadband absorption.

First, the metamaterial thermal emitter based on gold nanowire cavities is designed and analyzed to improve the overall efficiency of solar thermophotovoltaic (STPV) systems via optimizing the emission spectrum to be narrowband and with the emission peak located slightly above the bandgap of photovoltaic (PV) cells based on finite-element method simulations in COMSOL. The cavity resonant modes of both electric dipole and magnetic dipole are demonstrated in the metamaterial absorber and the temperature distribution by coupling the optical fields and thermal fields together is achieved. Theoretical analysis is performed to prove that the overall efficiency of the TPV system can reach Shockley–Queisser limit at a low emitter temperature of 940 K and even exceed Shockley-Queisser limit at higher temperature.

Second, a broadband perfect absorber made of ultrathin film working in visible and near-infrared (NIR) range is proposed and demonstrated. In theory, equations based on impedance transformation method are derived to guide the design; and in experiment, a silica-chromium-silica 3-layer absorber is fabricated to demonstrate the broadband perfect absorption. The measured absorption is above 90% over the wavelength range of 0.4–1.4 μm which matches the theory very well, and the absorber is angle-insensitive and polarization-independent.

Third, another broadband absorber covering the visible and near-infrared (NIR) is proposed firstly utilizing the combination of the multilayer impedance match in the short wavelength range and the double resonances in the long wavelength range. An equivalent circuit (EC) model is developed to analyze and optimize the ultrabroadband absorber according to the transmission line theory for the multilayer impedance and the coupled lumped-element LC resonators for the resonance impedance.

Finally, an ultra-broadband multilayer waveguide absorber is designed and studied via the stop light trapped at different waveguide width. The stop light mode is analyzed based on the waveguide mode theory considering the guided forward mode and backward mode at the same waveguide width position. An absorber sample is fabricated comprising of 13-pair gold and silicon dioxide layers, and the broadband absorption is measured by FTIR.

Each design mechanism makes the absorber tunable and controllable due to the accurate prediction in theory and simulation. The developed models and equations can guide the designing procedure and provide robust methods to further enhance the optical absorber performance.

BIBLIOGRAPHY

[1] R.M. Walser, "Electromagnetic metamaterials," Proc. SPIE. 4467, 1–15 (2001).

[2] http://www.darpa.mil/DARPATech2002/presentations/dso_pdf/speeches/BROWNING.pdf. Defense Advanced Research Projects Agency, (accessed Nov 11, 2014).

[3] N.I. Zheludev, "The road ahead for metamaterials," Science 328, 582–583 (2010).

[4] http://www.polymtl.ca/phys/doc/art_2_2.pdf, B. Ung, "Metamaterials: a metareview," (accessed Mar 26, 2014).

[5] W. Emerson, "Electromagnetic wave absorbers and anechoic chambers through the years," IEEE Transactions on Antennas and Propagation 21(4), 484-490 (1973).

[6] B. A. Munk, Frequency Selective Surfaces, John Wiley & Sons, New York (2000).

[7] W. W. Salisbury, US Patent 2599944 (1952).

[8] G. T. Ruck, D. E. Barrick, W. D. Stuart, Radar Cross Section Handbook, Vol. 2, Plenum, New York (1970).

[9] E. Knott, J. F. Shaeffer, M. T. Tuley, Radar Cross Section, Scitech, Raleigh (2004).

[10] J. E. Raynolds, B. A. Munk, J. B. Pryor, and R. J. Marhefka, "Ohmic loss in frequency-selective surfaces," Journal of Applied Physics 93(9), 5346-5358 (2003).

[11] R. M. Woodward, B. E. Cole and V. P. Wallace, "Terahertz pulse imaging in reflection geometry of human skin cancer and skin tissue," Phys. Med. Biol. 47, 3853–3863 (2002).

[12] J. W. Waters, L. Froidevaux and R. S. Harwood, "The earth observing system microwave limb sounder (EOS MLS) on the Aura Satellite," IEEE Transactions on Geoscience and Remote Sensing 44(5), 1075-1091 (2006).

[13] R. Appleby, "Standoff detection of weapons and contraband in the 100 GHz to 1 THz Region," IEEE Transactions on Antennas and Propagetion 55(11), 2944-2956 (2007).

[14] N. Nagai, M. Sumitomo, M Imaizumi, et al., "Characterization of electron- or proton-irradiated Si space solar cells by THz spectroscopy," Semicond. Sci. Technol. 21, 201–209 (2006).

[15] N. Dawahre, J. Brewer, G. Shen, et al., "Nanoscale characteristics of single crystal Zinc Oxide nanowires," 11th IEEE International Conference on Nanotechnology, USA, 640-645 (2011).

[16] N. I. Landy, S. Sajuyigbe, J. J. Mock, D. R. Smith, W. J. Padilla, "Perfect metamaterial absorber," Phys. Rev. Lett. 100, 207402 (2008).

[17] N. Laman, S. S. Harsha, D. Grischkowsky, et al., "High-resolution waveguide THz spectroscopy of biological molecules," Biophysical Journal 94, 1010–1020 (2008).

[18] D. Schurig, J. J. Mock and D. R. Smith, "Electric-field-coupled resonators metamaterials," App. Phys. Lett. 88, 041109-1-3 (2006).

[19] L. K. Sun, H. F. Cheng, Y. J. Zhou, et al, "Broadband metamaterial absorber based on coupling resistive frequency selective surface," Optics Express 20(4), 4675-4980 (2012).

[20] F. Alves, B. Kearney, D. Grbovic, et al., "Strong terahertz absorption using SiO2/Al based metamaterial structures," App. Phys. Lett. 100, 111104-1-3 (2012).

[21] J. Wu and W. Qin, "Terahertz dual-band nearly perfect absorbers based on combined of two types of FSS elements," Microwave Workshop Series on Millimeter Wave Wireless Technology and Applications (IMWS), IEEE MTT-S International, China (2012).

[22] H. T. Chen, J. f. Zhou, J. F. O'Hara, et al., "Antireflection coating using metamaterials and identification of its mechanism," PRL 105, 073901-4 (2010).

[23] H. T. Chen, J. f. Zhou, J. F. O'Hara, et al., "A numerical investigation of metamaterial antireflection coatings," Terahertz Science and Technology 3(2), 66-73 (2010).

[24] H. Tao, I. L. Landy, C. M. Bingham, et al., "A metamaterial absorber for terahertz regime: Design, fabrication and characterization," Optics Express 16(10), 7181-7188 (2008).

[25] Y. Zeng, H. T. Chen and D. A. R. Dalvit, "A reinterpretation of the metamaterial perfect absorber," arXiv: 1201.5109v1 (2012).

[26] X. Y. Peng, B. Wang, S. Lai, D. H. Zhang, et al., "Ultrathin multi-band planar metamaterial absorber based on standing wave resonances," Optics Express 20(25), 27756-27765 (2012).

[27] H. T. Chen, "Interference theory of metamaterial perfect absorbers," Optics Express 20(7), 7165-7172, (2012).

[28] Y. Ma, Q. Chen, Grant, J., Saha, et al., "A terahertz polarization insensitive dual band metamaterial absorber," Optics Letters 36(6), 945-947 (2011).

[29] X. Shen, T. J. Cui, J. Zhao, et al., "Polarization independent wide-angle triple-band metamaterial absorber," Optics Express 19(10), 9401-9407 (2011).

[30] H. Tao, C. M. Bingham, D. Pilon, et al., "A dual band terahertz metamaterial absorber," J. Phys. D: App. Phys. 43, 225102-7 (2010).

[31] X. Shen, Y. Yang, Y. Zang, et al., "Triple-band terahertz metamaterial absorber: Design, experiment, and physical interpretation," Appl. Phys. Lett. 101, 154102-1-4 (2012).

[32] Q. Ye, Y. Liu, H. Lin, et al., "Multi-band metamaterial absorber made of multi-gap SRRs structure," App. Phys. A 107, 155–160 (2012).

[33] L. Huang, R. D. Chowdhury, S. Ramani, et al., "Experimental demonstration of terahertz metamaterial absorbers with a broad and flat absorption band," Optics Letters 37(2), 154-156 (2012).

[34] Y. Q. Ye, Y. Jin and S. He, "Omnidirectional, polarization insensitive and broadband thin absorber in the terahertz regime," J. Opt. Soc. Am. B 27(3), 498-504 (2010).

[35] J. Sun, L. Liu, G. Dong and J. Zhou, "An extremely broadband metamaterial absorber based on destructive interference," Optics Express 19(22), 21156-21162 (2011).

[36] James Grant, Yong Ma, Shimul Saha, et al., "Polarization insensitive, broadband terahertz metamaterial absorber," Optics Letters 36(17), 3476-3478 (2011).

[37] Y. Liu, S. Gu, C. Luo, et al., "Ultra-thin broadband metamaterial absorber," Applied Physics A 108(1), 19-24 (2012).

[38] C. Zaichun, M. Rahmani, G. Yandong, et al., "Realization of variable three-dimensional terahertz metamaterial tubes for passive resonance tunability," Advanced Optical Materials 24(23), 143–147 (2012).

[39] H. Tao, A. C. Strikwerda, K. Fan, et al., "Terahertz metamaterials on free-standing highly-flexible polyimide substrates,". J. Phys. D: Appl. Phys. 41, 232004-1-5 (2008)

[40] W. Zhu, Y. Huang, I. D. Rukhlenko, et al., "Configurable metamaterial absorber with pseudo wideband spectrum," Optics Express 20(6), 6616-6621 (2012).

[41] L. Huang, D. Roy Chowdhury and S. Ramani, "Impact of resonator geometry and its coupling with ground plane on ultrathin metamaterial perfect absorbers," App. Phys. Lett. 101, 101102-1-4 (2012)

[42] J. Wang, C. Fan, P. Ding, et al., "Tunable broad-band perfect absorber by exciting of multiple plasmon resonances at optical frequency,". Optics Express 20(14), 14871-14878 (2012).

[43] H. Y. Zheng, X. R. Jin, J. W. Park, et al., "Tunable dual-band perfect absorbers based on extraordinary optical transmission and Fabry-Perot cavity resonance," Optics Express 20(21), 24003-24009 (2012)

[44] R. Siegel, J. R. Howell, Thermal Radiation Heat Transfer, Taylor & Francis, New York (2002).

[45] M. A. Green, K. Emery, Y. Hishikawa, W. Warta, E. D. Dunlop, "Solar cell efficiency tables (version 39)," Prog. Photovolt. 20, 12 (2012).

[46] B. Parida, S. Iniyan, R. Goic, Ren. Sust, "A review of solar photovoltaic technologies," Energ. Rev. 15, 1625 (2011).

[47] S. Bau, Y. B. Chen, Z. M. Zhang, "Microscale radiation in thermophotovoltaic devices - A review," Int. J. Energ. Res. 31, 689 (2007).

[48] J. van der Heide, Thermophotovoltaics, Elsevier, Leuven, Belgium (2012).

[49] R. Shukla, K. Sumathy, P. Erickson, J. Gong, Ren. Sust, "Recent advances in the solar water heating systems: A review," Energ. Rev. 19, 173 (2013).

[50] X. Liu, T. Tyler, T. Starr, A. F. Starr, N. M. Jokerst, W. J. Padilla, "Taming the Blackbody with Infrared Metamaterials as Selective Thermal Emitters," Phys. Rev. Lett. 107, 045901 (2011).

[51] H. Wang, L. Wang, "Perfect selective metamaterial solar absorbers," Opt. Exp. 21, A1078 (2013).

[52] P. Bouchon, C. Koechlin, F. Pardo, R. Haïdar, J. L. Pelouard, "Wideband omnidirectional infrared absorber with a patchwork of plasmonic nanoantennas," Opt. Lett. 37, 1038 (2012).

[53] S. Borri, P. Patimisco, A. Sampaolo, H. E. Beere, D. A. Ritchie, M. S. Vitiello, G. Scamarcio, "Terahertz quartz enhanced photo-acoustic sensor," Appl. Phys. Lett. 103, 02110 (2013).

[54] M. Hedayati, F. Faupel, M. Elbahri. "Tunable broadband plasmonic perfect absorber at visible frequency," Appl. Phys. A. 109, 769–773 (2012).

[55] F. Monticone, A. Alù, "Metamaterials and plasmonics: from nanoparticles to nanoantenna arrays, metasurfaces, and metamaterials," Chin. Phys. B. 23, 047809 (2014).

[56] H. Tao, N. I. Landy, C. M. Bingham, X. Zhang, R. D. Averitt, W. J. Padilla, "A metamaterial absorber for the terahertz regime: design, fabrication and characterization," Opt. Express. 16, 7181–7188 (2008).

[57] N. Liu, M. Mesch, T. Weiss, M. Hentschel, H. Giessen, "Infrared perfect absorber and its application as plasmonic sensor," Nano Lett. 10, 2342–2348 (2010).

[58] Y. Avitzour, Y. A. Urzhumov, G. Shvets, "Wide-angle infrared absorber based on a negative-index plasmonic metamaterial," Phys. Rev. B. 79, 045131 (2009).

[59] X. Liu, T. Tyler, T. Starr, A. F. Starr, N. M. Jokerst, W. J. Padilla, "Taming the blackbody with infrared metamaterials as selective thermal emitters,' Phys. Rev. Lett. 107, 045901 (2011).

[60] Y. Cui, K. H. Fung, J. Xu, H. Ma, Y. Jin, S. He, N. X. Fang, "Ultrabroadband light absorption by a sawtooth anisotropic metamaterial slab," Nano Lett. 12, 1443–1447 (2012).

[61] H. Sihvola, Electromagnetic Mixing Formulae and Applications, Institution of Electrical Engineers, London (1999).

[62] W. Shockley, and H. J. Queisser, "Detailed Balance Limit of Efficiency of p-n Junction Solar Cells," J. Appl. Phys. 32(3), 510–519 (1961).

[63] E. Rephaeli, and S. Fan, "Absorber and emitter for solar thermo-photovoltaic systems to achieve efficiency exceeding the Shockley-Queisser limit," Opt. Express 17(17), 15145–15159 (2009)

[64] C. Wu, B. Neuner, J. John, A. Milder, B. Zollars, S. Savoy, and G. Shvets, "Metamaterial-based integrated plasmonic absorber/emitter for solar thermo-photovoltaic systems," J. Opt. 14, 024005 (2012).

[65] S. Molesky, C. J. Dewalt, and Z. Jacob, "High temperature epsilon-near-zero and epsilon-near-pole metamaterial emitters for thermophotovoltaics," Opt. Express 21, A96-A110 (2013).

[66] X. Liu, T. Tyler, T. Starr, A. F. Starr, N. M. Jokerst, and W. J. Padilla, "Taming the blackbody with infrared metamaterials as selective thermal emitters," Phys. Rev. Lett. 107(4), 045901 (2011).

[67] J. A. Bossard, D. H. Werner, "Metamaterials with Custom Emissivity Polarization in the Near-Infrared," Opt. Express 21, 3872–3884 (2013).

[68] J. A. Bossard, D. H. Werner, "Metamaterials with Angle Selective Emissivity in the Near-Infrared," Opt. Express 21, 5215–5225 (2013).

[69] B. Lee, and Z. Zhang, "Design and fabrication of planar multilayer structures with coherent thermal emission characteristics," J. Appl. Phys. 100, 063529 (2006).

[70] G. Lévêque, and O.J.F. Martin, "Tunable composite nanoparticle for plasmonics," Opt. Letters 31(18), 2750–2752 (2006).

[71] K. Aydin, V. E. Ferry, R. M. Briggs, and H. A. Atwater, "Broadband polarization-independent resonant light absorption using ultrathin plasmonic super absorbers," Nat. Commun. 2, 517 (2011).

[72] Y. Ye, Y. Jin, and S. He, "Omnidirectional, polarization-insensitive and broadband thin absorber in the terahertz regime," J. Opt. Soc. Am. B 27, 498–504 (2010).

[73] W. Wang, et al., "Efficient multiband absorber based on one-dimensional periodic metal–dielectric photonic crystal with a reflective substrate," Opt. Letters 39(2), 331–334 (2014).

[74] J. Yu, Y. Shen, X. Liu, R. Fu, J. Zi, and Z. Zhu, "Absorption in one- -dimensional metallic-dielectric photonic crystals," Journal of Physics: Condensed Matter 16(7), L51–L56 (2004).

[75] S. Chen, et al., "Absorption enhancement in 1D Ag/SiO2 metallic-dielectric photonic crystals," Optica Applicata 39, 473–479 (2009).

[76] J.W. Dong, et al., "Robust absorption broadband in one-dimensional metallic-dielectric quasi-periodic structure," Opt. Express 14(5), 2014–2020 (2006).

[77] N. Mattiucci, M. J. Bloemer, N. Aközbek, and G. D'Aguanno, "Impedance matched thin metamaterials make metals absorbing," Sci. Rep. 3, 3203 (2013).

[78] Y. Cui, K. H. Fung, J. Xu, H. Ma, Y. Jin, S. L. He, and X. N. Fang, "Ultrabroadband light absorption by a sawtooth anisotropic metamaterial slab," Nano Lett 12(3), 1443–1447 (2012).

[79] F. Ding, et al., "Ultrabroadband strong light absorption based on thin multilayered metamaterials," Laser Photonics Rev. 8, 946–953 (2014).

[80] J. Zhou, A. F. Kaplan, L. Chen, L. J. Guo, "Experiment and theory of the broadband absorption by a tapered hyperbolic metamaterial array," ACS Photonics 1 (7), 618–624 (2014).

[81] D. Ji et al., "Broadband absorption engineering of hyperbolic metafilm patterns," Sci. Rep. 4, 4498 (2014).

[82] H.A. Haus, Waves and fields in optoelectronics, Englewood Cliffs, Prentice-Hall Inc., New Jersey (1984).

[83] E.D. Palik, Handbook of Optical Constants of Solids, Academic Press (1998).

[84] D. Barchiesi, and T. Grosges, "Fitting the optical constants of gold, silver, chromium, titanium, and aluminum in the visible bandwidth," Journal of Nanophotonics 8(1), 083097–083097 (2014).

[85] D. Rakic, A. B. Djurisic, J. M. Elazar, and M. L. Majewski, "Optical properties of metallic films for vertical-cavity optoe-lectronic devices," Appl. Opt. 37, 5271–5283 (1998).

[86] P. Buffat, J. P. Borel, "Size Effect on the Melting Temperature of Gold Particles," Phys. Rev. A 13, 2287–2298 (1976).

VITA

Huixu Deng received his Bachelor of Science degree in Mechanical Engineering in July 2011 from Huangzhong University of Science and Technology, Wuhan, China. In May 2018, he received his Doctor of Philosophy in Mechanical Engineering from Missouri University of Science and Technology, Rolla, Missouri, USA. His research interests focused on optical metamaterial absorber. During his Ph.D. study, he authored and co-authored 10 journal papers.